



aerosol_cci
IMARS ATBD

REF : IMARS-ATBD
ISSUE : 2.0
DATE : 12.12.2016
PAGE : 1



ESA Climate Change Initiative
aerosol_cci

**Infrared Mineral Aerosol Retrieval Scheme
(IMARS) Algorithm Theoretical Basis
Document (ATBD)**

Version 2.0

	aerosol_cci IMARS ATBD	REF : IMARS-ATBD ISSUE : 2.0 DATE : 12.12.2016 PAGE : 2
---	---	--

DOCUMENT STATUS SHEET

	FUNCTION	NAME	DATE	SIGNATURE
LEAD AUTHOR	editor	Lars Klüser	07.12.2016	
CONTRIBUTING AUTHORS				
REVIEWED BY	Science Leader	Gerrit de Leeuw	08.01.2017	
APPROVED BY	Technical officer (ESA)	Simon Pinnock		
ISSUED BY	Project manager	Thomas Holzer-Popp		

	aerosol_cci IMARS ATBD	REF : IMARS-ATBD ISSUE : 2.0 DATE : 12.12.2016 PAGE : 3
---	---	--

EXECUTIVE SUMMARY

The IMARS scheme is based on probabilistic estimation of the atmospheric state with respect to desert dust and ice clouds, based on pseudo-channel simulations of the observed signal for various dust and ice cloud properties. The solution to the radiative transfer problem is approximated by a generalized Two-Stream approach for spectrally resolved infrared radiative transfer. It is inspired by previous approaches for hyperspectral dust remote sensing in the terrestrial infrared. A total of 6000 brightness temperature difference sets (each being built from three pseudo-channel brightness temperatures) have been simulated with varying dust particle size distributions, mineralogical compositions, infrared optical depths and layer heights. The same amount of simulations has been performed for ice clouds. Based on a Gaussian distance metric the probability distribution function (PDF) over these 6000 realizations is determined and the state vector as well as its probability and uncertainty is estimated from the PDF. Optical properties have been obtained with the "Asymptotic Approximation Approach" (AAA) for non-spherical particles and have been evaluated with laboratory measurements of extinction spectra. Extinction and scattering efficiencies as well as asymmetry parameter and single scattering albedo have been pre-tabulated for each particle size distribution and mixture. Ice cloud optical properties have been compiled from a range of parameterizations found in the scientific literature as well as from AAA. The retrieval approach is followed sequentially for dust and ice clouds. Cloud screening is performed *a posteriori* based on probability and uncertainty estimates determined within the probabilistic retrieval itself. A quality flag for dust retrievals is included in the IMARS output together with pixelwise uncertainty estimates and the retrieval entropy, which is a concept borrowed from information theory describing the confidence in the cloud screening. The IMARS retrieval can be performed regardless of solar illumination as the contribution of reflected solar radiation to the observed spectra is extremely small. Also guidelines for IMARS product use are presented for four levels of quality filtering. The highest level of confidence in the IMARS results can be summarized as "trust everything with quality flag >3, dust probability >0.5, retrieval entropy <0.9 and uncertainty <40%". If sample size is more critical than absolute accuracy, it is advisable to release the filtering to "trust everything with quality flag >3 and retrieval entropy <0.9".

Issue	Date	Modified Items / Reason for Change
1.0	01.11.2014	First submission (IMARS v3.3)
2.0	12.12.2016	Considerable changes in algorithmic design and auxiliary data (IMARS v5.2)

LIST OF TABLES

Table 2.2-1: IASI spectral bands and covering spectral ranges	7
Table 4.3-1: Effective radius for the 12 dust representations used in IMARS. Dust mineralogical compositions as from Table 4.3-3.	14
Table 4.3-2: mass weighted mean diameter for the 12 dust representations used in IMARS. Dust mineralogical compositions as from Table 4.3-3.	14
Table 4.3-3: Typical desert dust compositional mixtures used in the IMARS retrieval. All relative mineral contributions are calculated by volume.....	14
Table 4.4-1: Mineralogical components and refractive index sources. For all minerals the refractive indices from the respective two sources have been averaged.	15
Table 5.4-1: Quality flag conditions in IMARS	31
Table 5.5-1: Quality flag conditions in IMARS	31
Table 6.2-1: Required auxiliary datasets for IMARS and corresponding currently used sources.....	37
Table 7.1-1: Output datasets contained in the generic IMARS output.....	38
Table 7.2-1:Dataset names and contained variables of the aerosol_cci IMARS output files.....	40
Table 8.1-1: Guidelines for application of different levels of quality filtering.	41
Table 8.2-1: Evaluation results for 2009 against AERONET SDA L1.5 observations.....	43
Table 8.2-2: Evaluation results for 2009 against AERONET SDA L2.0 observations.....	43

LIST OF FIGURES

Figure 2.1-1: Design of the Metop EPS satellites. © EUMETSAT	5
Figure 2.2-1: Schematic view of the IASI measurement principle and FOV alignment. © CNES.	6
Figure 2.2-2: IASI specified and theoretical spectral resolution (from http://smc.cnes.fr/IASI/spectral_res.htm) © CNES	7
Figure 4.2-1: Full spectral resolution (blue) and binned-maximum-brightness-temperature (red) spectra of the IASI instrument for cases with (bottom) and without (top) desert dust signal. The pristine cases (i.e. no dust signal) are depicted for low (left) and high (right) water vapour content whereas the dust cases show spectra over ocean (left) and over desert (right) in order to illustrate the impact of surface emissivity.	11
Figure 4.2-2: Degrees of Freedom for Signal as a function of dust AOD and dust layer temperature (left) and the dust information spectrum in the atmospheric window region (right).....	12
Figure 4.4-1: Extinction efficiency (top), single scattering albedo (middle) and asymmetry parameter (bottom) for quartz (left) and illite (right) as simulated with the AAA method (blue) and Lorenz- Mie theory (red) as well as corresponding laboratory measurements of the University of Iowa (black) in the terrestrial IR spectral region. The spectra and size distributions correspond to the measurements described in [RD14].....	21
Figure 4.4-2: Extinction efficiency spectra of kaolinite rich (top) and illite and quartz rich (bottom) dust samples as simulated with the AAA method (blue) and Lorenz-Mie theory (black) as well as corresponding laboratory measurements of the University of Paris East (red) in the terrestrial IR window region. The figures correspond to dust extinction directly after injection into the atmospheric simulation chamber (left) and after 50 minutes residence time (right) and consequently to different size distributions as larger particles deposit faster (see [RD41]).....	22
Figure 4.5-1: Example of simulated brightness temperature differences for various TIR AODs. These simulations have been performed with the “Iowa Loess” mixture and the lognormal “Aerosol_cci” particle size distribution for ocean (left) and desert (right) surface emissivities and for near-surface dust (approx. 500m, top) and an elevated dust layer (approx. 5km, bottom).....	23
Figure 4.5-2: Example of simulated brightness temperature differences for various TIR ice cloud optical depths. These simulations have been performed for ocean surface emissivities at a moderate cloud height of (approx. 5km, bottom). Brightness temperature differences have been simulated for ice cloud with an effective diameter of 40µm with the parameterizations of <i>Yang et al. 2005</i> (top left), <i>Baum et al. 2013</i> (top right), and the AAA disk model (bottom left). For the latter also the impact of crystal size of the BTD is exemplarily presented for simulations with an effective radius of 80µm.	25
Figure 5.1-1: Overview of the IMARS processing environment.	27
Figure 5.4-1: Program flow chart of the IMARS retrieval. The retrieval loop is repeated for all FOVs per scanline and for all scanlines of the granule/orbit. This flow chart is a close-up of the blue box in Figure 5.1-1.	29
Figure 5.4-2: Modular design of the IMARS version 5.2 algorithm chain, independently performed for each FOV. This module plot is a schematic close-up of the white box (“imars_loop”) in Figure 5.4-1.....	30
Figure 5.6-1: IMARS results for P_{dust} (top left) and P_{cloud} (top right) and H (bottom left) as well as dust AOD _{0.55µm} (bottom right) for the large dust outbreak off the coast of West Africa on 17 September 2010 observed with IASI on board Metop-A.	32
Figure 5.6-2: IMARS results for dust N_{var} (top left) and illite abundance (top right) as well as the two size distribution representations R_{eff} (bottom left) and D_{mv} (bottom right) for the large dust outbreak off the coast of West Africa on 17 September 2010 observed with IASI on board Metop-A.	33

Figure 5.6-3: IMARS results for P_{dust} (top left), ε_{dust} (top right), dust N_{var} (middle left) dust quality flag (middle right), dust $AOD_{0.55\mu m}$ (bottom left) and AOD ratio between $0.55\mu m$ and $10\mu m$ (bottom right) for a dust outbreak from the Asian deserts on 21 March 2010 observed with IASI on board Metop-A. 35

Figure 8.2-1: IMARS dust AOD evaluation results against AERONET SDA L2.0 coarse mode AOD in terms of scatter plots (left) and deviation histograms (right) for all observations (top) and quality-filtered observations (bottom). Observations of 73 AERONET stations for the year 2009 have been used for comparison. 44



TABLE OF CONTENTS

DOCUMENT STATUS SHEET	II
EXECUTIVE SUMMARY	III
LIST OF TABLES	IV
LIST OF FIGURES	V
TABLE OF CONTENTS.....	VII
1 INTRODUCTION	1
1.1 Scope.....	1
1.2 References.....	1
1.2.1 Applicable Documents.....	1
1.2.2 Reference Documents.....	1
2 IASI INSTRUMENT CHARACTERISTICS	5
2.1 The Metop satellites.....	5
2.2 IASI instrument overview.....	6
3 SCOPE OF THE PROBLEM.....	8
4 SCIENTIFIC BACKGROUND.....	9
4.1 Infrared resonance bands of mineral dust.....	9
4.2 Radiative transfer modelling and spectral aggregation.....	9
4.3 Physico-chemical characteristics of desert dust.....	13
4.4 Optical properties of non-spherical desert dust particles.....	14
4.5 Theoretical considerations of the IMARS retrieval approach.....	22
5 IMPLEMENTATION	27
5.1 IMARS processing environment.....	27
5.2 Preparatory steps.....	28
5.3 Surface emissivity.....	28
5.4 Implementation of the core dust retrieval.....	28
5.5 Quality Flags.....	30
5.6 A posteriori cloud discrimination and approval of results.....	31
5.7 Retrieval examples.....	32
6 INPUT DATA REQUIREMENTS.....	36
6.1 IASI LIC data.....	36
6.2 Auxiliary data.....	36
7 ALGORITHM OUTPUT	38
7.1 Generic IMARS output.....	38
7.2 IMARS aerosol_cci specific output.....	39
8 GENERAL REMARKS AND PRODUCT QUALITY	41

	<p style="text-align: center;">aerosol_cci IMARS ATBD</p>	<p>REF : IMARS-ATBD ISSUE : 2.0 DATE : 12.12.2016 PAGE : 8</p>
---	---	--

8.1 Guidelines for product use: confidence levels41

8.2 Estimated accuracy from evaluation by the developer.....42

9 CONCLUDING REMARKS 46

	aerosol_cci IMARS ATBD	REF : IMARS-ATBD ISSUE : 2.0 DATE : 12.12.2016 PAGE : 1
---	---	--

1 INTRODUCTION

This document describes the theoretical basis for the mineral dust aerosol retrieval algorithm developed by DLR-DFD for the IASI (Infrared Atmospheric Sounding Interferometer) instruments on board of EUMETSAT's Metop satellites. This algorithm is referred to as IMARS (Infrared Mineral Aerosol Retrieval Scheme).

1.1 Scope

This ATBD aims to provide an overview of the IMARS algorithm with detailed references, with summaries of the issues that are important for the Aerosol_cci work and specifically the IMARS retrieval scheme. It will not be a comprehensive compilation of all existing literature on the topic of hyperspectral infrared aerosol retrieval.

The currently used and herein described retrieval implementation refers to version 5.2 of the IMARS algorithm. Version 5 distinguishes itself from all lower versions in that it is no longer based on principle component decomposition of simulated (or observed) IASI spectra but that forward simulations with different dust AOD and dust layer altitude (in terms of thermal contrast between ground and dust) are evaluated in a probabilistic way in order to acquire dust information from the IASI observations. Moreover, due to high redundancy in the IASI spectra, it uses four pseudo-channels centered at central wavelengths of typical narrowband imaging instruments.

Scientific publications referred to within this document describe earlier algorithm versions and do not necessarily reflect the latest changes (also those within Aerosol_cci as an outcome of the project work) implemented into the scheme and documented within this ATBD. All references to IMARS within Aerosol_cci should thus include the citation of the latest issue of this ATBD.

1.2 References

1.2.1 Applicable Documents

- [AD1] Statement of Work "ESA Climate Change Initiative Stage 1, Scientific user Consultation and Detailed Specification", ref EOP-SEP/SOW/0031-09/SP. Issue 1.4, revision 1, dated 9 November, 2009, together with its Annex C "Aerosols" (altogether the SoW).
- [AD2] The Prime Contractor's Baseline proposal, ref. 3003432, Revision 1.0, dated 16 June 2010, and the minutes of the July 26, 2010 kick-off meeting
- [AD3] ESA Climate Change Initiative, aerosol_cci, Product Specification Document, Version 3.0, ref Aerosol_cci2_PSD. Issue 3.0, dated 14 December 2016.

1.2.2 Reference Documents

- [RD1] Mahowald, N.M., Kloster, S., Engelstaedter, S., Moore, J.K., Mukhopadhyay, S., McConnell, J.R., Albani, S., Doney, S.C., Bhattacharya, A., Curran, M.A.J., Flanner, M.G., Hoffman, F.M., Lawrence, D.M., Lindsay, K., Mayewski, P.A., Neff, J.,



- Rothenberg, D., Thomas, E., Thornton, P.E., and Zender, C.S.: Observed 20th century desert dust variability: impact on climate and biogeochemistry, *Atm. Chem. Pys.*, 10, 10875-10893, doi: 10.5194/acp-10-10875-2010, 2010.
- [RD2] Clarisse, L., Coheur, P.-F., Prata, F., Hadji-Lazaro, J., Hurtmans, D., and Clerbaux, C.: A unified approach to infrared aerosol remote sensing and type specification, *Atmos. Chem. Phys.*, 13, 2195-2221, 2013.
- [RD3] Caquineau, S., Gaudichet, A., Gomes, L., Magonthier, M.-C., and Chatenet, B.: Saharan dust: Clay ratio as a relevant tracer to assess the origin of soil-derived aerosols, *Geophys. Res. Lett.*, 25, 983-986, 1998.
- [RD4] Formenti, P., Rajot, J.L., Desboeufs, K., Caquineau, S., Chevaillier, S., Nava, S., Gaudichet, A., Journet, E., Triquet, S., Alfaro, S., Chiari, M., Haywood, J., Coe, H., and Highwood, E.: Regional variability of the composition of mineral dust from western Africa: Results from the AMMA SOP0/DABEX and DODO field campaigns, *J. Geophys. Res.*, 113, D003C134, doi:10.1029/2008JD009903, 2008.
- [RD5] Kandler, K., Schütz, L., Jäckel, S., Lieke, K., Emmel, C., Müller-Ebert, D., Ebert, M., Scheuven, D., Schladitz, A., Šegvić, B., Wiedensohler, A., and Weinbruch, S.: Ground-based off-line aerosol measurements at Praia, Cape Verde during the Saharan Mineral Dust Experiment: microphysical properties and mineralogy, *Tellus*, 63B, 459-474, 2011.
- [RD6] Ackerman, S.A.: Remote sensing aerosols using satellite infrared observations, *J. Geophys. Res.*, 102, 17069-17079, 1997.
- [RD7] Sokolik, I.N., and Toon, O.B.: Incorporation of mineralogical composition into models of the radiative properties of mineral aerosol from UV to IR wavelengths, *J. Geophys. Res.*, 104, D8, 9423-9444, 1999.
- [RD8] Klüser, L., Banks, J.R., Martynenko, D., Bergemann, C., Brindley, H.E., and Holzer-Popp, T.: Information content of space-borne hyperspectral infrared observations with respect to mineral dust properties, *Remote Sensing of Environment*, 156, 204-309, doi:10.1016/j.rse.2014.09.036, 2015.
- [RD9] Laskina, O., Young, M.A., Kleiber, P.D., and Grassian, V.H.: Infrared extinction spectra of mineral dust aerosol: Single components and complex mixtures, *J. Geophys. Res.*, doi:10.1029/2012JD017756, 2012.
- [RD10] Hudson, P. K., Gibson, E.R., Young, M. A., Kleiber, P. D., and Grassian, V. H.: Coupled infrared extinction and size distribution measurements for several clay components of mineral dust aerosol, *J. Geophys. Res.*, 113, D01201, doi:10.1029/2007JD008791, 2008a.
- [RD11] Hudson, P. K., Young, M. A., Kleiber, P. D., and Grassian, V. H.: Coupled infrared extinction spectra and size distribution measurements for several non-clay components of mineral dust aerosol (quartz, calcite, and dolomite), *Atm. Environ.*, 42, 5991-5999, 2008b.
- [RD12] Klüser, L., Kleiber, P., Holzer-Popp, T., and Grassian, V.H.: Desert dust observation from space – Application of measured mineral component infrared extinction spectra, *Atm. Env.*, 54, 419-427, 2012.
- [RD13] Yang, P., Feng, Q., Hong, G., Kattawar, G.W., Wiscombe, W.J., Mishchenko, M.I., Dubovik, O., Laszlo, I., and Sokolik, I.N.: Modeling of the scattering and radiative properties of nonspherical dust-like aerosols, *Journal of Aerosol Science*, 28, 995-1014, 2007.



- [RD14] Mogili, P.K., Yang, K.H., Young, M.A., Kleiber, P.D., and Grassian, V.H.: Extinction spectra of mineral dust aerosol components in an environmental aerosol chamber: IR resonance studies, *Atm. Env.*, 42, 1752-1761, 2008.
- [RD15] De Leeuw, G., et al.: Evaluation of seven European aerosol optical depth retrieval algorithms for climate analysis, *Remote Sens. Environ.*, doi:10.1016/j.rse.2013.04.023, 2015.
- [RD16] Legrand, M., Dubovik, O., Lapyonok, T. Derimian, Y., Accounting for particle non-sphericity in modeling of mineral dust radiative properties in the thermal infrared, *J. Quant. Spectrosc. Radiat. Transf.*, 149, 219-240, doi:10.1016/j.jqsrt.2014.07.014, 2014.
- [RD17] Bohren, C.F., and Huffman, D.R., Absorption and scattering of light by small particles, John Wiley & Sons, New York, USA, 1983.
- [RD18] Chýlek, P., Asymptotic limits of the Mie-scattering characteristics, *J. Opt. Soc. Am. A*, 65, 1316-1323, 1975.
- [RD19] Acquista, C., Cohen, A., Cooney, J.A., Wimp, J., Asymptotic behaviour of the efficiencies in Mie scattering, *J. Opt. Soc. Am.*, 70, 1023-1028, 1980.
- [RD20] v.d. Hulst, H.C., Light scattering by small particles, Dover Publications, Inc., New York, USA, 1980.
- [RD21] Di Biagio, C., Boucher, H., Caqueneau, S., Chevaillier, S., Cuesta, J., and Formenti, P.: Variability of the infrared complex refractive index of African mineral dust: experimental estimation and implications for radiative transfer and satellite remote sensing, *Atmos. Chem. Phys.*, 14, 11093–11116, doi:10.5194/acp-14-11093-2014, 2014.
- [RD22] Wenrich, M.L., and Christensen, P.R.: Optical constants of minerals derived from emission spectroscopy: application to quartz, *J. Geophys. Res.*, 101, B7, 15921-15931, 1996.
- [RD23] Glotch, T.D., Rossman, G.R., and Aharonson, O.: Mid-infrared (5-100 μ m) reflectance spectra and optical constants of ten phyllosilicate minerals, *Icarus*, 192, 605-622, 2007.
- [RD24] Querry, M.R., Optical constants of minerals and other materials from the millimeter to the ultraviolet, US Army, Aberdeen, Md, USA, 1987.
- [RD25] Roush, T., Pollack, J., Orenberg, J., Derivation of midinfrared (5-25 μ m) optical constants of some silicates and palagonite, *Icarus*, 94, 191-208, 1991.
- [RD26] Lane, M.D., Midinfrared optical constants of calcite and their relationship to particle size effects in the thermal emission spectra of granular calcite, *J. Geophys. Res.*, 104/E6, 14099-14108, 1999.
- [RD27] Aronson, J.R., Emslie, A.G., Smith, E.M., and Strong, P.F.: Infrared spectra of lunar soils and related optical constants, *Proc. Lunar Planet. Sci. Conf. 10th*, 1787-1795, 1979.
- [RD28] Long, L.L., Querry, M.R., Bell, R.J., Alexander, R.W, Optical properties of calcite and gypsum in crystalline and powdered form in the infrared and far-infrared, *Infrared Phys.*, 34, 191-201, 1993.
- [RD29] Aronson, J.R.: Optical constants of monoclinic anisotropic crystals: orthoclase, *Spectrochimica Acta*, 42A, 187-190, 1986.
- [RD30] Yang, P., Wei, H., Huang, H.-L., Baum, B.A., Hu, Y.X., Kattawar, G.W., Mishchenko, M.I., and Fu, Q.: Scattering and absorption property database for nonspherical ice particles in the near- through far-infrared spectral region, *Appl. Opt.*, 44, 5512-5523, 2005.



- [RD31] Lentz, W.J.: Generating Bessel functions in Mie scattering calculations using continued fractions, *Appl. Opt.*, 15, 668-671, 1976.
- [RD32] D. Deirmendjian, *Electromagnetic Scattering on Spherical Polydispersions*, RAND Report R-456-PR, Elsevier, New York, 1969.
- [RD33] Spitzer, W.G., and Kleinman, D.A.: Infrared lattice bands of quartz, *Phys. Rev.*, 121, 1324-1335, doi:10.1103/PhysRev.121.1324, 1961.
- [RD34] Shannon, C.E, *Communication in the Presence of Noise*, *Proceedings of the IEEE*, 86, 2, 447-457, 1949.
- [RD35] Shannon, C.E., and Weaver, W.: *The Mathematical Theory of Communication*, University of Illinois Press, 1949.
- [RD36] Chýlek, P., Klett, J.D., Absorption and scattering of electromagnetic radiation by prismatic columns: anomalous diffraction approximation, *J. Opt. Soc. Am. A*, 8(11), 1713-1720, 1991.
- [RD37] Maslowska, A., Flatau, P.J., Stephens, G.L., On the validity of the anomalous diffraction theory to light scattering by cubes, *Opt. Commun.*, 107, 35-40, 1994.
- [RD38] Yang, P., Wei, H., Huang, H.-L., Baum, B.A., Hu, Y.X., Kattawar, G.W., Mishchenko, M.I., Fu, Q., Scattering and absorption property database for nonspherical ice particles in the near- through far-infrared spectral region, *Appl. Opt.*, 44, 5512-5523, 2005.
- [RD39] Baum, B.A., Yang, P., Heymsfield, A.J., Bansemer, A., Cole, B.H., Merrelli, A., Schmitt, C., and Wang, C.: Ice cloud single-scattering property models with the full phase matrix at wavelengths from 0.2 to 100 μm , *Journal of Quantitative Spectroscopy & Radiative Transfer*, 146, 123–139, doi: 10.1016/j.jqsrt.2014.02.029, 2014.
- [RD40] Petty, G.W.: *A First Course in Atmospheric Radiation*, Sundog Publishing, Madison, Wisconsin, USA, 2006.
- [RD41] Klüser, L., Di Biagio, C., Kleiber, P.D., Formenti, P., and Grassian, V.H.: Optical properties of non-spherical desert dust particles in the terrestrial infrared – An asymptotic approximation approach, *J. Quant. Spectrosc. Radiative Transf.*, 178, 209-223, doi:10.1016/j.jqsrt.2015.11.020, 2016.
- [RD42] Rodgers, C.D.: *Inverse methods for atmospheric sounding, theory and practice*, Series on atmospheric, oceanic and planetary physics, vol.2, World Scientific Publishing, Singapore, 2000.
- [RD43] O'Neill, N.T., Ecki, T.F., Smirnov, A., Holben, B.N., and Thulasiraman, S.: Spectral discrimination of coarse and fine mode optical depth, *J. Geophys. Res.*, 108, D17, 4559, doi:10.1029/2002JD002975, 2003.

	aerosol_cci IMARS ATBD	REF : IMARS-ATBD ISSUE : 2.0 DATE : 12.12.2016 PAGE : 5
---	---	--

2 IASI INSTRUMENT CHARACTERISTICS

2.1 The Metop satellites

The European Polar System (EPS) consists of three Metop satellites with Metop-A in orbit since October 2006 and Metop-B since 2012. The launch of Metop-C is scheduled for 2018. EPS is the European contribution to the Initial Joint Polar System (IJPS) agreed upon by EUMETSAT and NOAA. Details can be found at:

<http://www.eumetsat.int/website/home/Satellites/CurrentSatellites/Metop/index.html>

The European and American satellites of the IJPS carry a set of identical sensors: AVHRR/3, AMSU-A, HIRS/4 and MHS.

The European EPS satellites as well carry an additional set of sensors: IASI, ASCAT, GOME-2 and GRAS. Moreover they operate the Argos Advanced Data Collection System (A-DCS). The design of the Metop satellites is depicted in figure 2.1-1. Equator crossing time of the EPS satellites is 09:30 local solar time at an altitude of 817km and an inclination of 98.7°.

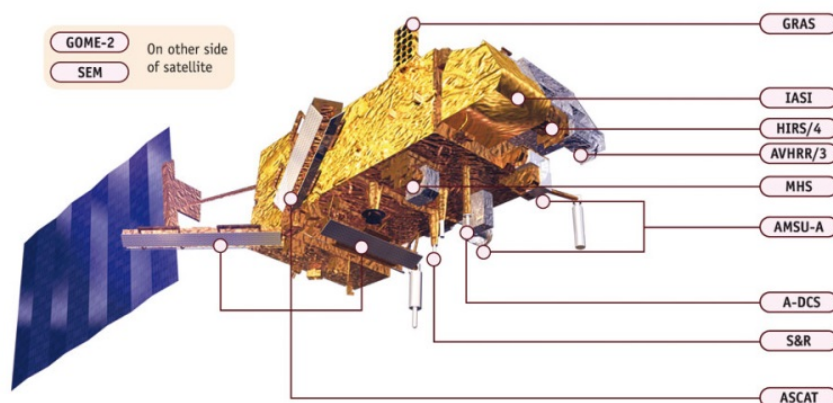


Figure 2.1-1: Design of the Metop EPS satellites. © EUMETSAT

	aerosol_cci IMARS ATBD	REF : IMARS-ATBD ISSUE : 2.0 DATE : 12.12.2016 PAGE : 6
---	---	--

2.2 IASI instrument overview

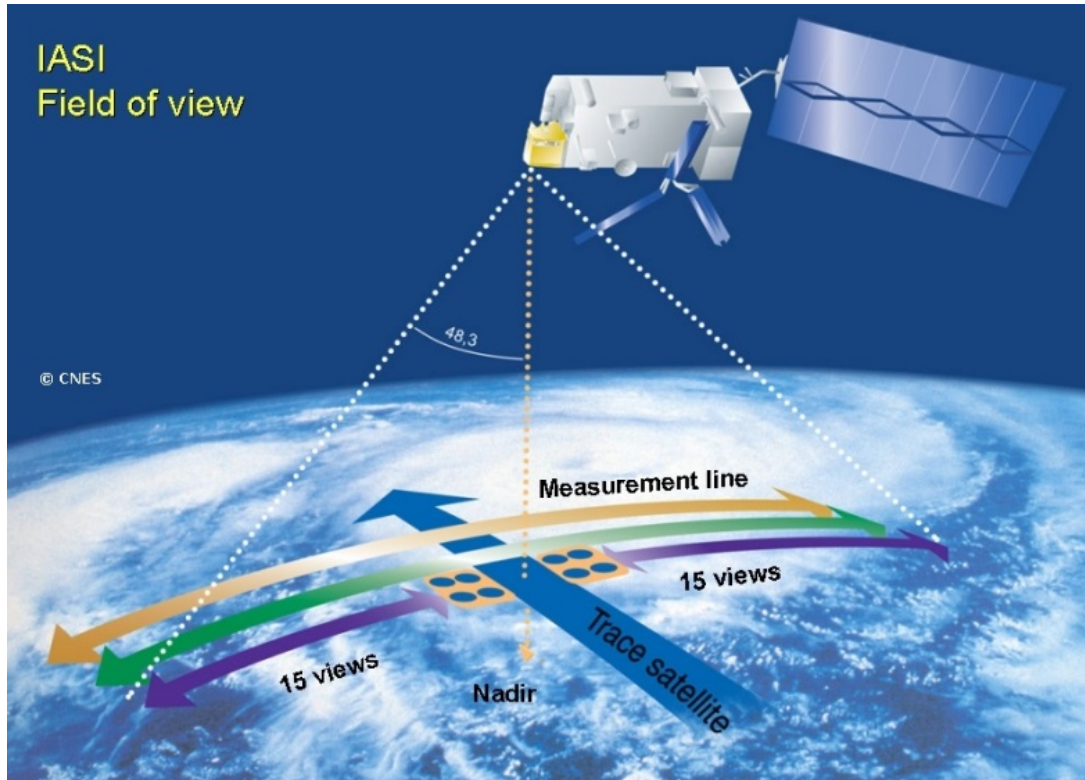


Figure 2.2-1: Schematic view of the IASI measurement principle and FOV alignment.
© CNES.

On board of the Metop satellites is the Infrared Atmospheric Sounding Interferometer (IASI), a scanning Michelson interferometer with very fine spectral resolution in the terrestrial infrared designed for observation of atmospheric temperature and humidity profiles. It observes infrared radiance spectra in the $3.7\mu\text{m} - 15.5\mu\text{m}$ spectral range (in three overlapping bands, Table 2.2-1) at 12km nadir ground resolution and a swath of 48.3° (2200km). It scans the earth with four detectors simultaneously and each swath (scanline) is divided into 30 2x2 scan matrices, i.e. each scanline contains 60 fields-of-view (FOV). The scan principle is shown in figure 2.2-1 schematically. The ground resolution of 12km is a tradeoff between radiometric performance and the statistical likelihood of valid measurement acquisition in dependence of cloud cover.

8461 channels in the terrestrial infrared result in a spectral resolution of $<0.5\text{cm}^{-1}$ (figure 2.2-2). Instrument stability is very high, namely 0.3K at an absolute accuracy of 0.5K. The spectral resolution of apodized L1C spectra is 0.5cm^{-1} over the entire spectrum.



Table 2.2-1: IASI spectral bands and covering spectral ranges

Band	Range (cm ⁻¹)	Range (μm)
1	645 to 1210	15.5 to 8.26
2	1210 to 2000	8.26 to 5
3	2000 to 2760	5 to 3.62

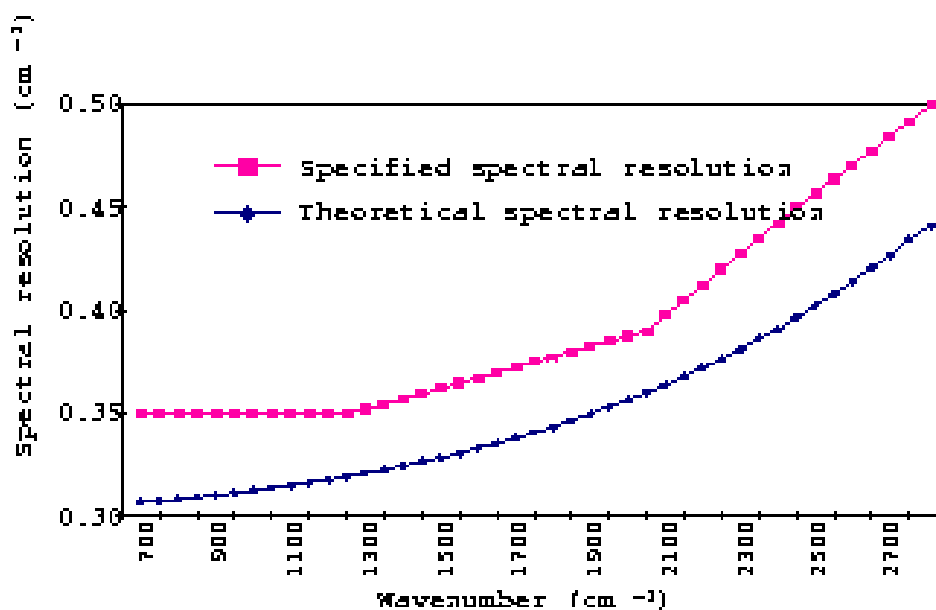


Figure 2.2-2: IASI specified and theoretical spectral resolution
(from http://smc.cnes.fr/IASI/spectral_res.htm) © CNES

	aerosol_cci IMARS ATBD	REF : IMARS-ATBD ISSUE : 2.0 DATE : 12.12.2016 PAGE : 8
---	---	--

3 SCOPE OF THE PROBLEM

Mineral dust in the atmosphere has gained increased scientific interest during recent years owing to its important role in the climate system and its impacts on air quality. Airborne dust interacts directly with solar and terrestrial radiation. Dust particles can also act as cloud condensation nuclei or ice nuclei, altering cloud microphysical and optical properties. Both direct and indirect effects alter the radiation balance, and thus atmospheric and surface heating. Dust from the Sahara, the largest dust source in the world, also acts as an important source of iron for maritime biogeochemistry (e.g. [RD1]).

In the terrestrial infrared (TIR) it is possible to detect a couple of aerosol types (e.g. [RD2]). The detectable aerosol types with highest atmospheric abundance and mass load together with the highest impacts for environment and climate are desert dust and volcanic ash. They are generally well detectable in TIR due to Si-O and other resonance bands dramatically increasing absorption and scattering in the TIR. Moreover particle sizes of dust and volcanic ash are sufficiently large for resulting in sufficiently high volume extinction, so that the signal can be extracted from TIR observations.

The IMARS algorithm provides an estimate of the dust AOD (aerosol optical depth) in TIR as well as an estimate of the visible dust AOD based on the retrieved dust particle size and composition. Moreover mass columns and dust layer effective emission temperature are retrieved alongside. The IMARS data can be used to assess the atmospheric dust load as well as to function as prior or posterior estimate of the aerosol type for other retrieval algorithms.

In TIR dust remote sensing, the problems to deal with are different from those in aerosol retrieval at solar wavelengths. The radiation source is the earth's surface as well as the atmosphere itself. Contribution of (reflected) solar radiation to the TIR radiance observed from space is extremely small. As a consequence the atmospheric profile plays a crucial role in determining the radiance observed by TIR satellite instruments. The surface leaving radiance is additionally governed by the surface emissivity, which over sparsely vegetated land areas causes significant problems. Also the absorption (and consequently also emission) by gases, mainly water vapour and ozone, further complicate the retrieval problem. As if all this were not enough, the dust itself shows a large variability in optical properties depending on particle size, particle shape and dust composition. All these determine the absorption and scattering properties as well as the thermal emission by the dust itself. Exact treatment of all these strongly varying parameters would cause computational costs not feasible within any retrieval algorithm, thus any TIR dust retrieval algorithm has to make (partly critical) assumptions and simplifications.

	aerosol_cci IMARS ATBD	REF : IMARS-ATBD ISSUE : 2.0 DATE : 12.12.2016 PAGE : 9
---	---	--

4 SCIENTIFIC BACKGROUND

This section summarizes the main physical principles underlying the IMARS algorithm, whereas its implementation is summarized in Section 5.

4.1 Infrared resonance bands of mineral dust

The majority of airborne mineral dust is composed of silicate minerals like quartz or silicate clays. Moreover carbonates and sulfates as well as iron oxides are commonly found in mineral dust samples (e.g.[RD3]-[RD5]).

Silicates are characterised by strong $\nu(Si-O)$ vibrational stretch resonance bands around 1050cm^{-1} [$9.5\mu\text{m}$]. Layered aluminosilicates like kaolinite also show a significant secondary $\delta(Al-Al-OH)$ vibrational resonance band around 920cm^{-1} (see e.g. [RD2]).

Although maximum extinction of TIR radiation by silicates is observed around 1050cm^{-1} [$9.5\mu\text{m}$], the peak extinction is masked by the strong O_3 absorption band around 1040cm^{-1} [$9.6\mu\text{m}$]. But as the broad silicate resonance band shoulders stretch to outside the O_3 absorption band, the the extinction signal still can be detected from space-borne TIR observations (e.g.[RD6]).

The iron oxides hematite and limonite/goethite exhibit a weak resonance band at 1025cm^{-1} which is only 2% of the intensity of $Si-O$ resonance in this region. Thus the iron oxide absorption is generally masked by silicate peaks in airborne dust and cannot be detected from TIR satellite observations ([RD7]).

As a consequence spectral characteristics of dust extinction have to be known or assumed for extracting quantitative dust information from TIR instruments (see details in section 4.3). The strong impact of variable assumptions about dust infrared optical properties on retrieval results from IASI has been shown in [RD8].

4.2 Radiative transfer modelling and spectral aggregation

The azimuthally averaged form of the spectral radiative transfer equation for thermal infrared radiation including scattering as formulated e.g. in [RD6] is

$$\mu \frac{dI(\tau, \nu, \mu)}{d\tau} = I(\tau, \nu, \mu) - (1 - \omega_0(\nu)) \cdot B_\nu(T(\tau)) - \left(\frac{\omega_0(\nu)}{2} \right) \cdot \int_0^\mu P_s(\tau, \nu, \mu, \mu') \cdot I(\tau, \nu, \mu') d\mu' \quad (1)$$

where μ is the cosine of the viewing angle, τ is optical depth, $I(\tau, \nu, \mu)$ is the incident radiation, $B_\nu(T)$ represents the Planck function for given temperature T , ω_0 is the single scattering albedo defined by β_{scat}/β_{ext} (with $\beta_{ext} = \beta_{scat} + \beta_{abs}$) and P_s is the scattering phase function.

With knowledge of spectrally resolved optical depth ($\tau(\nu)$), single scattering albedo ($\omega_0(\nu)$) and asymmetry parameter ($g(\nu)$), the effective transmissivity of the dust can be simulated with a discrete-ordinates approach to the Two-Stream solution of the

	aerosol_cci IMARS ATBD	REF : IMARS-ATBD ISSUE : 2.0 DATE : 12.12.2016 PAGE : 10
---	---	---

radiative transfer equation including atmospheric scattering (eq. (4-1)), but neglecting multiple scattering between the surface and the dust layer.

Using L_{\downarrow} , the downwelling spectral radiance at the top-of-atmosphere (negligible in TIR) and $L_{\uparrow} = \varepsilon_{sfc} B_{\nu}(T_{sfc})$ with surface temperature T_{sfc} , the upwelling spectral radiance at the surface, as boundary conditions and furthermore assume isotropic emission by the surface and the dust layer (assumed isothermal with temperature T_{dust}), the Two-Stream solution of the radiative transfer problem can be formulated as ([RD40])

$$I_{sat}(\nu) = \left(R(\nu) + \frac{A_{sfc}(\nu)T_{gas}(\nu)T(\nu)^2}{1-A_{sfc}(\nu)R(\nu)} \right) L_{\downarrow}(\nu) + \frac{T_{gas}(\nu)T}{1-A_{sfc}(\nu)R(\nu)} L_{\uparrow}(\nu) + T_{gas}(\nu)A(\nu) \cdot B_{\nu}(T_{dust}) \quad (2)$$

In this formulation A_{sfc} is the surface albedo ($=1 - \varepsilon_{sfc}$ by Kirchhoff's law, as the transmissivity of the solid earth can be regarded as being zero), T_{gas} the atmospheric transmissivity due to gas absorption, A is the absorptivity of the dust layer, R is the reflectivity of the dust layer and T is the transmissivity of the dust layer. The latter three quantities are calculated using

$$\Gamma(\nu) = 2\sqrt{1 - \omega_0(\nu)}\sqrt{1 - g(\nu)\omega_0(\nu)} \quad (3)$$

and

$$R_{\infty}(\nu) = \frac{\sqrt{1-g(\nu)\omega_0(\nu)} - \sqrt{1-\omega_0(\nu)}}{\sqrt{1-g(\nu)\omega_0(\nu)} + \sqrt{1-\omega_0(\nu)}} \quad (4)$$

as

$$R(\nu) = R_{\infty}(\nu) \frac{e^{\Gamma(\nu)\tau(\nu)} - e^{-\Gamma(\nu)\tau(\nu)}}{e^{\Gamma(\nu)\tau(\nu)} - R_{\infty}(\nu)^2 e^{-\Gamma(\nu)\tau(\nu)}} \quad (5)$$

$$T(\nu) = \frac{1 - R_{\infty}(\nu)^2}{e^{\Gamma(\nu)\tau(\nu)} - R_{\infty}(\nu)^2 e^{-\Gamma(\nu)\tau(\nu)}} \quad (6)$$

$$A(\nu) = 1 - R(\nu) - T(\nu) \quad (7)$$

where $\tau(\nu)$ is the dust AOD envisaged to be retrieved by IMARS. It is clearly evident, that eq. (1) cannot simply be inverted and solved for $\tau(\nu)$. The IMARS scheme exploits IASI radiances in the atmospheric window in the 8-12 μ m domain (825 cm^{-1} -1250 cm^{-1}).

In order to avoid contamination by narrow gas absorption lines the radiances are collected into bins of 10 IASI channels each. Then the channel with the highest brightness temperature per bin is assumed to be least affected by the atmospheric state. This assumption works fine for small single absorption lines but is not entirely true at the edge of the water vapour continuum (see Fig. 4.2-1). Consequently in moist conditions the uncertainty of the dust signal increases. Thus from 420 channels between 833 cm^{-1} and 1250 cm^{-1} 42 spectral bins are derived. Among those, seven bins are highly contaminated by strong O_3 absorption and are not used, resulting in 35 spectral bins

used in the dust retrievals ([RD12]). Figure 4.2-1 illustrates the maximum brightness temperature binning and the selection of spectral bins around the O₃ absorption band.

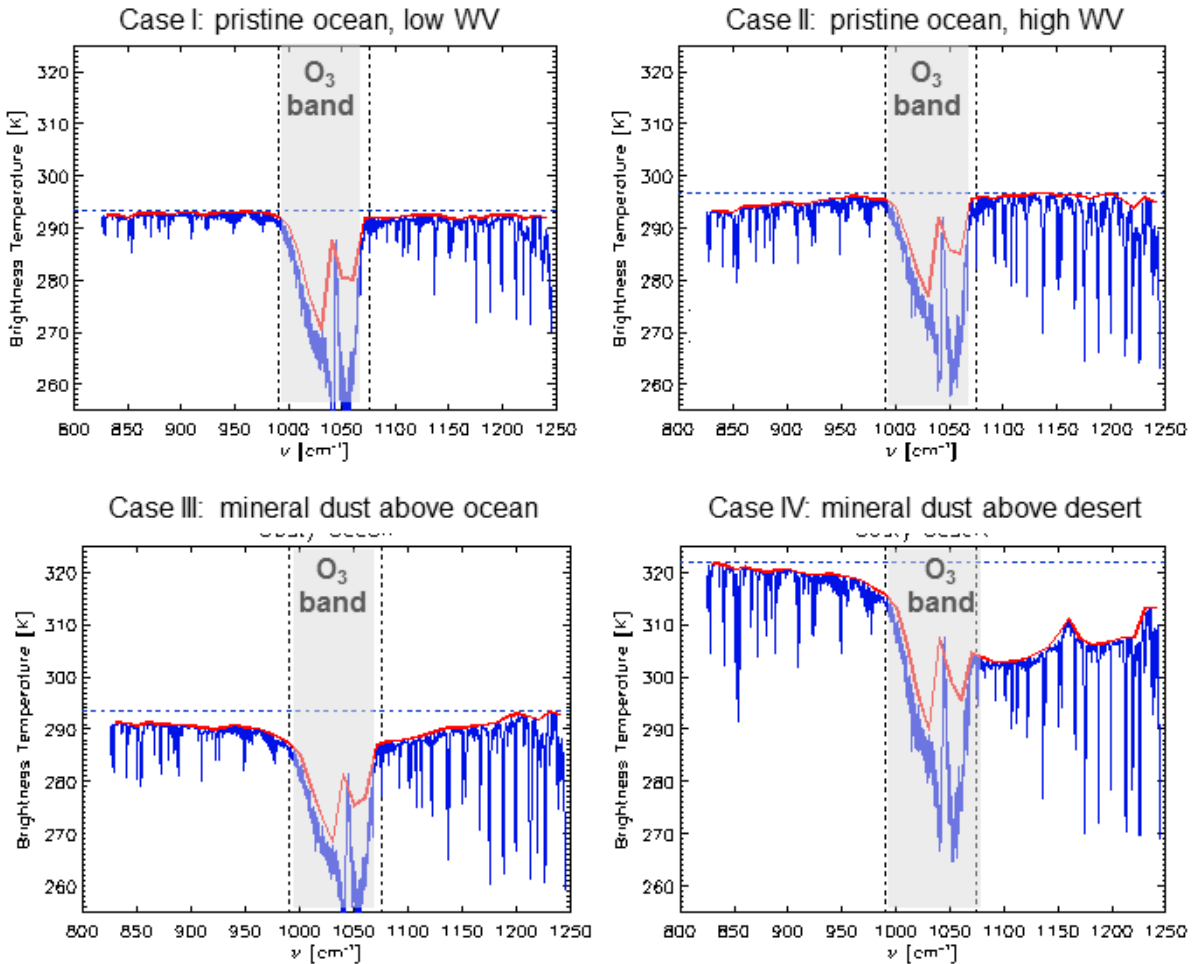


Figure 4.2-1: Full spectral resolution (blue) and binned-maximum-brightness-temperature (red) spectra of the IASI instrument for cases with (bottom) and without (top) desert dust signal. The pristine cases (i.e. no dust signal) are depicted for low (left) and high (right) water vapour content whereas the dust cases show spectra over ocean (left) and over desert (right) in order to illustrate the impact of surface emissivity.

Information content analysis of these spectra simulated with different sets of optical dust properties shows a maximum of more than 5 degrees of freedom for signal (DFS) and a mean of around 3 to 4 (Figure 4.2-2).

Degrees of freedom for signal are calculated from the eigenvalues λ of the covariance matrix of the spectrum as ([RD42])

$$DFS = \sum_i \frac{\lambda_i^2}{1 + \lambda_i^2} \tag{8}$$

	aerosol_cci IMARS ATBD	REF : IMARS-ATBD ISSUE : 2.0 DATE : 12.12.2016 PAGE : 12
---	---	---

The information content is not equally distributed over the spectrum, but is highest near the *Si-O* resonance peak and drops significantly towards the outward boundaries of the window region (Figure 4.2-2). The information spectrum ([RD8], [RD42]) is based on the *information content* or information entropy H ([RD34], [RD35]) and is evaluated for all spectral bins j as the sum over the histogram p (realized with 50 bins) of the brightness temperature values for the respective bin. Brightness temperature spectra have been simulated for a wide range of dust properties (composition and size distribution), dust AOD and dust layer height (see subsequent chapters for details).

$$\forall j \in [1,35]: H(j) = -\sum_{i=1}^{50} p_i(T_i[j]) \cdot \log_2(p_i(T_i[j])) \quad (9)$$

The information content analysis reveals a high redundancy amongst the 35 spectral bins. Consequently IMARS processing time can be decreased by subselection or aggregation into 3-6 information channels. Channel selection is partly based on the information spectrum (Figure 4.2-2) and partly on considerations of potential wider application possibilities for IMARS.

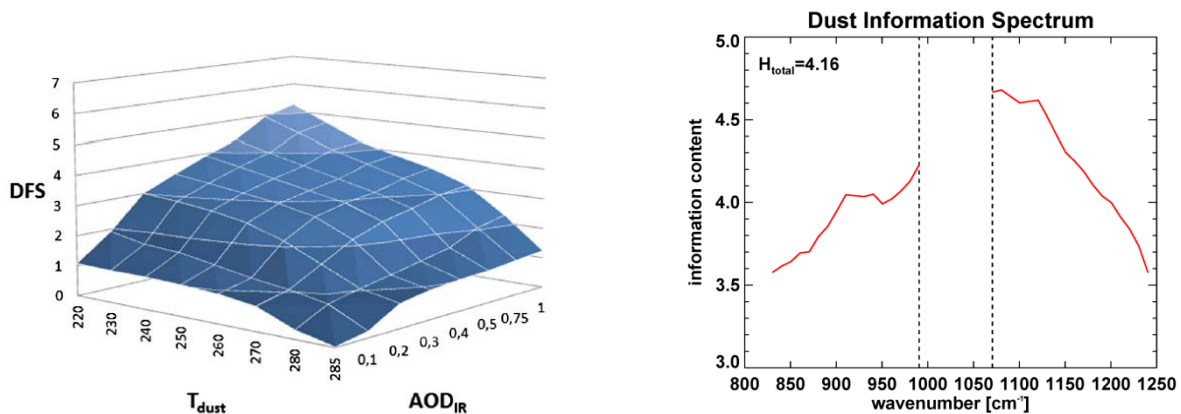


Figure 4.2-2: Degrees of Freedom for Signal as a function of dust AOD and dust layer temperature (left) and the dust information spectrum in the atmospheric window region (right).

Consequently, in IMARS v5.2 from these 35 bins 28 are aggregated into three pseudo-channels mimicking the three TIR window channels of narrow-band imaging instruments such as the *Spinning Enhanced Visible and InfraRed Imager* (SEVIRI) on board of the Meteosat Second Generation satellites or the *MODerate resolution Imaging Spectro-radiometer* (MODIS) on the US Earth Observation Satellites (EOS) "Aqua" and "Terra". The aggregation is performed by collecting 14 bins (with minimized gas absorption signal) into one pseudo-channel centered at 1149.5cm^{-1} ($8.7\mu\text{m}$) and reflecting a channel band width of $0.8\mu\text{m}$. Furthermore 10 bins are collected into a pseudo-channel centered at 926.0cm^{-1} ($10.8\mu\text{m}$, channel width of $1.0\mu\text{m}$) and 4 bins at the lower end of the wavenumber spectrum represent a pseudo-channel of $0.5\mu\text{m}$

	aerosol_cci IMARS ATBD	REF : IMARS-ATBD ISSUE : 2.0 DATE : 12.12.2016 PAGE : 13
---	---	---

width centered at 840cm^{-1} ($11.9\mu\text{m}$). For simplicity, the brightness temperatures of these three pseudo-channels are referred to as T_{08} , T_{11} and T_{12} in the remainder of this document.

In order to reduce the amount of required forward simulations brightness temperatures of the three pseudo channels in both, observations and simulations, are scaled to a normal basis of 293.15K. For the scaling first the baseline temperature is calculated as the maximum of the three pseudo-channel brightness temperatures

$$T_{base} = \max\{T_{08}, T_{11}, T_{12}\} \quad (10)$$

Then each of the three pseudo-channel brightness temperatures is scaled according to

$$T_{\lambda}^* = B_{\lambda}^{-1} \left(B_{\lambda}[T_{\lambda}] \frac{B_{\lambda}[T_{base}]}{B_{\lambda}[293.15K]} \right) \quad (11)$$

The star (*) annotating scaled brightness temperatures is omitted for the remainder of this document as all brightness temperatures used throughout the rest of the document will always be scaled brightness temperatures.

The three pseudo-channel brightness temperatures are collected into a set of four brightness temperature differences reflecting the spectral variation of the dust (or cloud or surface) signal:

$$BTD_1 = T_{08} - 2T_{11} + T_{12} \quad (12)$$

$$BTD_2 = T_{11} - T_{12} \quad (13)$$

$$BTD_3 = T_{08} - T_{12} \quad (14)$$

$$BTD_4 = T_{08} - T_{11} \quad (15)$$

4.3 Physico-chemical characteristics of desert dust

The very high variability in particle size, particle shape and mineralogical composition of Aeolian dust has strong consequences for infrared optical properties (e.g. [RD7], [RD13]). For IMARS version 5.2 three different size distributions and four representative mineralogical dust mixtures are used. The size distributions represent the mono-modal dust particle size distribution used in the solar algorithms of Aerosol_cci ([RD15]), as well as two size distributions describing the dust samples used for atmospheric simulation chamber measurements ([RD14], [RD21], [RD41]). These describe one size distribution of dust sampled in an active dust source region ("China1" from [RD41], described in detail in [RD21]) dominated by rather coarse particles and one size distribution determined from the individual contributions of dust components as described in [RD14]. Consequently both size distributions representing laboratory measurements account for domination of different particle modes by different mineralogical components of the dust. Moreover, as the absorption spectra samples by the University of Iowa (referred to as "Iowa" size distribution in the following) have been acquired for single mineral samples with individual size distributions, the resulting size distribution of the "Iowa" class is different for each mineralogical mixture ([RD41]). The combination of four

	aerosol_cci IMARS ATBD	REF : IMARS-ATBD ISSUE : 2.0 DATE : 12.12.2016 PAGE : 14
---	---	---

mixtures and three size distributions yields a set of 12 dust representations with different size distributions. Table 4.3-2 lists the corresponding effective radii, Table 4.3-1 the corresponding mass-weighted mean diameter D_{mw} (see e.g. [RD14], [RD41]) and Table 4.3-3 the mineralogical compositions of the three dust mixtures used in IMARS. The contribution from iron oxides and other heavy minerals has been neglected as the impact on TIR spectra is usually negligible and thus no information about these can be reliably obtained from TIR observations.

Table 4.3-1: Effective radius for the 12 dust representations used in IMARS. Dust mineralogical compositions as from Table 4.3-3.

	China	Central Sahara	Niger	Iowa Loess
Aerosol_cci	1.93 μm	1.93 μm	1.93 μm	1.93 μm
LISA	2.76 μm	2.76 μm	2.76 μm	2.76 μm
Iowa	1.33 μm	1.45 μm	0.76 μm	1.96 μm

Table 4.3-2: mass weighted mean diameter for the 12 dust representations used in IMARS. Dust mineralogical compositions as from Table 4.3-3.

	China	Central Sahara	Niger	Iowa Loess
Aerosol_cci	5.53 μm	5.53 μm	5.53 μm	5.53 μm
LISA	7.63 μm	7.63 μm	7.63 μm	7.63 μm
Iowa	7.77 μm	7.51 μm	5.18 μm	10.09 μm

Table 4.3-3: Typical desert dust compositional mixtures used in the IMARS retrieval. All relative mineral contributions are calculated by volume.

mixture	Ref.	quartz	illite	kaolinite	montm.	feldsp.	calcite
China	[RD21]	21.6%	28.5%	8.5%	14.2%	0.0%	27.7%
C. Sahara	[RD9]	1.4%	31.3%	16.2%	33.6%	8.8%	8.7%
Niger	[RD21]	27.2%	6.9%	64.4%	0.0%	0.0%	1.5%
Iowa Loess	[RD9]	0.0%	17.9%	0.0%	69.8%	11.4%	0.9%

4.4 Optical properties of non-spherical desert dust particles

Table 4.4-1 lists refractive indices used for the mineralogical components in the generation of infrared optical properties. In the case of birefringent minerals (quartz and calcite) a ratio of 2:1 for the ordinary and extraordinary rays is used (e.g. [RD33]) for averaging the optical constants before the calculation of the optical properties.

	aerosol_cci IMARS ATBD	REF : IMARS-ATBD ISSUE : 2.0 DATE : 12.12.2016 PAGE : 15
---	---	---

Table 4.4-1: Mineralogical components and refractive index sources. For all minerals the refractive indices from the respective two sources have been averaged.

Component	Abbreviation	Refractive index reference
Quartz	Qz	[RD33] <i>Spitzer and Kleinman (1961)</i> [RD22] <i>Wenrich and Christensen (1996)</i>
Illite	Il	[RD23] <i>Glotch et al. (2007)</i> [RD24] <i>Querry (1987)</i>
Kaolinite	Ka	[RD24] <i>Querry (1987)</i> [RD25] <i>Roush et al. (1991)</i>
Montmorillonite	Mo	[RD24] <i>Querry (1987)</i> [RD25] <i>Roush et al. (1991)</i>
Calcite	Ca	[RD26] <i>Lane (1999)</i> [RD28] <i>Long et al. (1993)</i>
Feldspars	Fs	[RD27] <i>Aronson et al. (1979)</i> [RD29] <i>Aronson (1986)</i>

Several studies analyzed the usefulness of Lorenz-Mie theory for estimation of dust optical properties in the TIR (e.g. [RD8], [RD12], [RD13], [RD30]) with dramatically differing results. Lorenz-Mie solutions for light scattering spheres consist of calculating extinction and scattering efficiencies Q_{ext} and Q_{scat} , respectively, by

$$Q_{ext} = \frac{2}{x^2} \sum_{n=1}^{\infty} (2n+1) \text{Re}(a_n + b_n) \quad (16)$$

$$Q_{scat} = \frac{2}{x^2} \sum_{n=1}^{\infty} (2n+1) (|a_n|^2 + |b_n|^2) \quad (17)$$

The Mie coefficients (a_n and b_n) depend on the complex refractive index m as well as on the size parameter $x=2\pi r/\lambda$ (where r describes the particle radius and λ the wavelength of the incident light) and are thus spectral quantities. Especially for small particles the numerical solutions of Mie solvers become unstable ([RD31], [RD32]). Moreover the effects of non-sphericity result in additional non-negligible uncertainty (e.g. [RD8], [RD14], [RD16]).

A method for determining optical properties of non-spherical particles with arbitrary size distribution is the asymptotical combination of Rayleigh limit (i.e. small particle) solutions with geometric optics (i.e. large particle) solutions. This approach, termed "Asymptotic Approximation Approach" (AAA) has been described and evaluated in full detail in [RD41]. Its basic theoretical foundations are outlined in this section.

For particles in the Rayleigh limit ($x \ll 1$) scattering can widely be neglected and the extinction efficiency is resembled by the particle absorption only. For non-spherical particles different approximations of Rayleigh limit absorptions have been formulated ([RD14], [RD10], [RD11], [RD17]).

	aerosol_cci IMARS ATBD	REF : IMARS-ATBD ISSUE : 2.0 DATE : 12.12.2016 PAGE : 16
---	---	---

Generally absorption and scattering efficiencies in the small particle limit can be described by the polarizability α ([RD17]):

$$Q_{abs,\alpha} = \frac{4}{3} x \text{Im}(\alpha) \quad (18)$$

$$Q_{scat,\alpha} = \frac{16}{162} x^4 |\alpha|^2 \quad (19)$$

In the preparation of optical properties for non-spherical particles the radius r in x is assumed to be represented by the radius of a volume equivalent sphere for the respective particle, which allows to use the size parameter x in the calculations.

Of interest for desert dust particles are mainly the solutions for the "Continuous Distribution of Ellipsoids" (CDE) and the "Disk" approximations ([RD10], [RD11], [RD14], [RD17]). The respective absorption efficiencies are then

$$Q_{abs,CDE} = \frac{4}{3} x \text{Im} \left(\frac{2m^2}{m^2 - 1} \log[m^2] \right) \quad (20)$$

$$Q_{abs,disk} = \frac{4}{9} x \left(\frac{1}{(\text{Re}[m^2])^2 + (\text{Im}[m^2])^2} + 2 \right) \text{Im}[m^2] \quad (21)$$

As both are linear in x , the solutions are formally valid approximation only for $x \ll 1$ (in the Rayleigh limit) Corresponding scattering efficiencies for small ellipsoidal particles can be calculated by

$$Q_{scat,CDE} = \frac{16}{162} x^4 \left| \frac{2m^2 \log(m^2)}{m^2 - 1} \right|^2 \quad (22)$$

$$Q_{scat,disk} = \frac{16}{162} x^4 |m^2 - 1|^2 \left(\frac{1}{(\text{Re}[m^2])^2 + (\text{Im}[m^2])^2} + 2 \right) \quad (23)$$

Similar Rayleigh-limit solutions for the absorption and scattering efficiencies can also be derived for needle-shaped and spherical particles ([RD17]).

The scattering phase function in the Rayleigh limit is represented by the Rayleigh phase function

$$P_{Rayleigh}(\cos \theta) = \frac{3}{4} (1 + \cos^2 \theta) \quad (24)$$

	aerosol_cci IMARS ATBD	REF : IMARS-ATBD ISSUE : 2.0 DATE : 12.12.2016 PAGE : 17
---	---	---

The asymmetry parameter

$$g = \int_{-1}^1 P(\cos(\theta)) \cos(\theta) d \cos(\theta) \quad (25)$$

is constantly zero in the Rayleigh limit as this is the analytical solution from the Rayleigh phase function. Moreover in the Rayleigh limit the scattering efficiency, being a function of x^4 , is typically very small, thus the Rayleigh limit contribution to anisotropic scattering is extremely small.

In the large particle limit the Mie solutions show an asymptotic behavior and tend to approximate an analytic solution (e.g. [RD18], [RD19]). The asymptotic limit for Mie scattering of large spherical particles is

$$Q_{scat,lim} = 1 + \left| \frac{m-1}{m+1} \right|^2 \quad (26)$$

In the large particle limit the radius of curvature of the sphere approaches infinity. Thus in the large particle limit all spheres can also be interpreted by Fresnel reflection on flat surfaces (which have curvature radius of infinity). The asymptotic Mie limit presented by [RD19] suggests $Q_{ext,lim}=2$ regardless of absorption and thus fails to reproduce strong absorption bands. This approximation cannot reliably reproduce the optical properties of the strongly absorbing Reststrahlen bands of for example silicate particles.

For any incidence angle ϕ the complex angle of refraction is defined by ([RD17])

$$\cos(\phi') = \frac{\cos(\phi)}{m} \quad (27)$$

and the Fresnel reflection coefficients are

$$r_1(\phi) = \frac{\sin(\phi) - m \cdot \sin(\phi')}{\sin(\phi) + m \cdot \sin(\phi')} \quad (28)$$

$$r_2(\phi) = \frac{m \cdot \sin(\phi) - \sin(\phi')}{m \cdot \sin(\phi) + \sin(\phi')} \quad (29)$$

The Fresnel reflectance of a large particle (i.e. x approaches infinity) follows from eq. (28) and eq. (29) as

$$R(\phi) = \frac{1}{2} \left(|r_1(\phi)|^2 + |r_2(\phi)|^2 \right) \quad (30)$$

The transmission of an infinitely large particle becomes zero and the scattering efficiency then can be expressed by the angular integral over the Fresnel reflection ([RD20]):



$$Q_{scat,Fresnel} = 1 + 2 \int_0^{\pi/2} R(\phi) \sin \phi \cos \phi d\phi \quad (31)$$

where the first summand is the diffraction efficiency and the second summand (the integral) describes the reflection at the (particle) surface. In the limiting case of perpendicular incidence the Fresnel reflection approach is equal to the asymptotic Mie solution for large particles.

The Fresnel transmittance can likewise be calculated from

$$t_1(\phi) = \frac{2 \sin(\phi)}{\sin(\phi) + m \cdot \sin(\phi')} \quad (32)$$

$$t_2(\phi) = \frac{2 \sin(\phi)}{m \cdot \sin(\phi) + \sin(\phi')} \quad (33)$$

as

$$T(\phi) = \frac{1}{2} (|t_1(\phi)|^2 + |t_2(\phi)|^2) \quad (34)$$

The Fresnell solution is used to calculate the path of individual rays at the particle surfaces for large particles. The extinction and absorption efficiencies of optically soft particles (i.e. diffraction not accounting for strong reflection at the particle surface) can also be estimated with the Anomalous Diffraction Theory (ADT) ([RD20], [RD36], [RD37]):

$$Q_{ext,ADT} = 4 \operatorname{Re} \left(\frac{1}{2} - \frac{\exp(-2xi \cdot (m-1))}{2x \cdot (m-1)} + \frac{\exp(-2xi \cdot (m-1)) - 1}{(2x \cdot (m-1))^2} \right) \quad (35)$$

$$Q_{abs,ADT} = 1 - 2 \frac{\exp(-4x \cdot \operatorname{Im}(m))}{4x \cdot \operatorname{Im}(m)} + 2 \frac{\exp(-4x \cdot \operatorname{Im}(m)) - 1}{(4x \cdot \operatorname{Im}(m))^2} \quad (36)$$

The scattering efficiency is not directly determined with the ADT, but results from the difference between extinction and absorption. The approach is equivalent to the estimation of the absorption from the Lorenz-Mie solutions. The main advantage of using the ADT solution is that Q_{ext} and Q_{abs} can be estimated without assumptions about the particle shape. Strictly speaking ADT is only valid for particles with $|m|x-1 \approx 0$ (optically soft particles), but that constraint mainly relates to the phase lag of the electromagnetic wave inside the particle and thus for the scattered (diffracted) ray. [RD36] nevertheless argue that the errors introduced by deviations from this conditions significantly decrease with increasing absorption. Consequently, it can be assumed that they are of minor importance near strong resonance absorption bands like those of silicate dust in the TIR.

	aerosol_cci IMARS ATBD	REF : IMARS-ATBD ISSUE : 2.0 DATE : 12.12.2016 PAGE : 19
---	---	---

As ADT mainly considers the diffraction of the light and does not reliably account for reflection at the particle surface, the scattering efficiency for large particles, including diffraction and reflection, can be approximated by combining eq. (28), eq. (29) and eq. (30) and substituting the diffraction term in eq. (31) by the corresponding ADT solution:

$$Q_{scat,A+F} = (Q_{ext,ADT} - Q_{abs,ADT}) + \int_0^{\pi/2} R(\phi) \sin \phi \cos \phi d\phi \quad (37)$$

The scattering phase function for the large particle approximation can be calculated from combining eq. (24), eq. (30) and the angular diffraction pattern ([RD17]). The diffraction contribution is calculated as ([RD20])

$$P_{diff}(\theta) = (1 - e^{-i\rho \sin \phi}) \cdot J_0(x\theta \cos \phi) \cdot \sin \phi \cdot \cos \phi \quad (38)$$

where J_0 is the zero-order Bessel function, ϕ is the incidence angle as above and the scattering angle θ for the transmitted ray is

$$\theta = 2(\phi - \phi') \quad (39)$$

The combined phase function for the asymptotic large particle approximation then becomes

$$P_{A+F}(\theta) = P_{diff}(\theta) + R(\phi, \phi') + T(\phi, \phi') + (1 - R(\phi, \phi'))^2 \cdot T(\phi, \phi')^2 \quad (40)$$

where ϕ and ϕ' determine the scattering angle θ according to the number of external and internal reflections.

A generalized solution for extinction and absorption by non-spherical particles is derived from combining the asymptotic Rayleigh and large particle approximations described above. While in the Rayleigh approximations the absorption efficiency is directly linear in x (eq. (20) and (21)), in the large particle limit the Fresnel solutions for extinction, scattering and absorption efficiencies are functions of m and the incidence angle only whereas the ADT solutions show a more complex dependence on x , but no angular dependence. One way to combine the different solutions without strictly separating by size parameter thresholds is to use a weighting function which is nonlinear in x , bound to [0,1] and asymptotically approaches 0 for small x and 1 for large x . This can be achieved by weighting of the two asymptotic solutions with an exponential decay function in the form

$$\begin{bmatrix} f_1 \\ f_2 \end{bmatrix} = \begin{bmatrix} 1 - e^{-y} \\ e^{-y} \end{bmatrix} \quad (41)$$

Acknowledging that the validity of the Rayleigh approximation generally requires $x \ll 1$ whereas the validity of the geometric optics solution generally requires $x \gg 1$, there is

	aerosol_cci IMARS ATBD	REF : IMARS-ATBD ISSUE : 2.0 DATE : 12.12.2016 PAGE : 20
---	---	---

good reasoning for postulating that both approaches shall be exactly equally weighted at $x=1$. The equality $f_1(y_0) = f_2(y_0)$ is valid exactly at $y_0 = -\ln(0.5)$. Thus

$$y = -x \cdot \ln\left(\frac{1}{2}\right) = x \cdot \ln(2) \quad (42)$$

in eq. (41). Strictly speaking the Rayleigh approaches are valid only for $x \ll 1$, while the error of the Fresnel + ADT solution decreases as x approaches infinity. Thus both methods are good representations of the asymptotic behavior of extinction spectra in the small and large particle limits. Combining the Rayleigh and Fresnel + ADT solutions by f_1 respective f_2 yields the "Asymptotic Approximation Approach" (AAA) for arbitrary refractive index and particle size:

$$Q_{abs}(m, x) = f_1(x) \cdot Q_{abs,ADT}(m, x) + f_2(x) \cdot Q_{abs,Rayleigh}(m, x) \quad (43)$$

$$Q_{scat}(m, x) = f_1(x) \cdot Q_{scat,A+F}(m, x) + f_2(x) \cdot Q_{scat,Rayleigh}(m, x) \quad (44)$$

The Rayleigh limit method to be used (CDE or disk) depends on the mineral component (see [RD12], [RD14]). Extinction efficiency and single scattering albedo are obtained from $Q_{ext} = Q_{scat} + Q_{abs}$ and $\omega_0 = Q_{scat}/Q_{ext}$, respectively. The scattering phase function is calculated by

$$P(\theta) = \frac{e^{-x \ln(2)} \cdot Q_{scat,Rayleigh} \cdot P_{Rayleigh}(\theta) + (1 - e^{-x \ln(2)}) \cdot Q_{scat,A+F} \cdot P_{A+F}(\theta)}{Q_{scat,Rayleigh} + Q_{scat,A+F}} \quad (45)$$

where m and x dependences are omitted for the sake of readability.

In a comparison study with laboratory extinction measurements of dispersed mineral dust ([RD41]) the AAA method for calculating the optical properties of non-spherical particles of arbitrary size has shown very good agreement with the measurements.

Examples for dust extinction spectra calculated with traditional Mie theory, with the AAA method and the corresponding laboratory measurements (all from [RD41]) are shown for quartz and illite in Figure 4.4-1. Also the corresponding spectra of single scattering albedo and asymmetry parameter are shown.

Analogously Figure 4.4-2 shows extinction spectra of kaolinite-rich ("Niger") and illite/quartz-rich ("China") bulk dust samples in the terrestrial infrared window region as simulated with the AAA method, with Lorenz-Mie theory as well as measurements from an atmospheric simulation chamber (as described in [RD41]). The two spectra for each mixture reflect the evolution of the spectral extinction during the residence time within the chamber (see [RD21]). These spectra clearly highlight the benefit of the AAA method for hyperspectral TIR remote sensing ([RD41]).

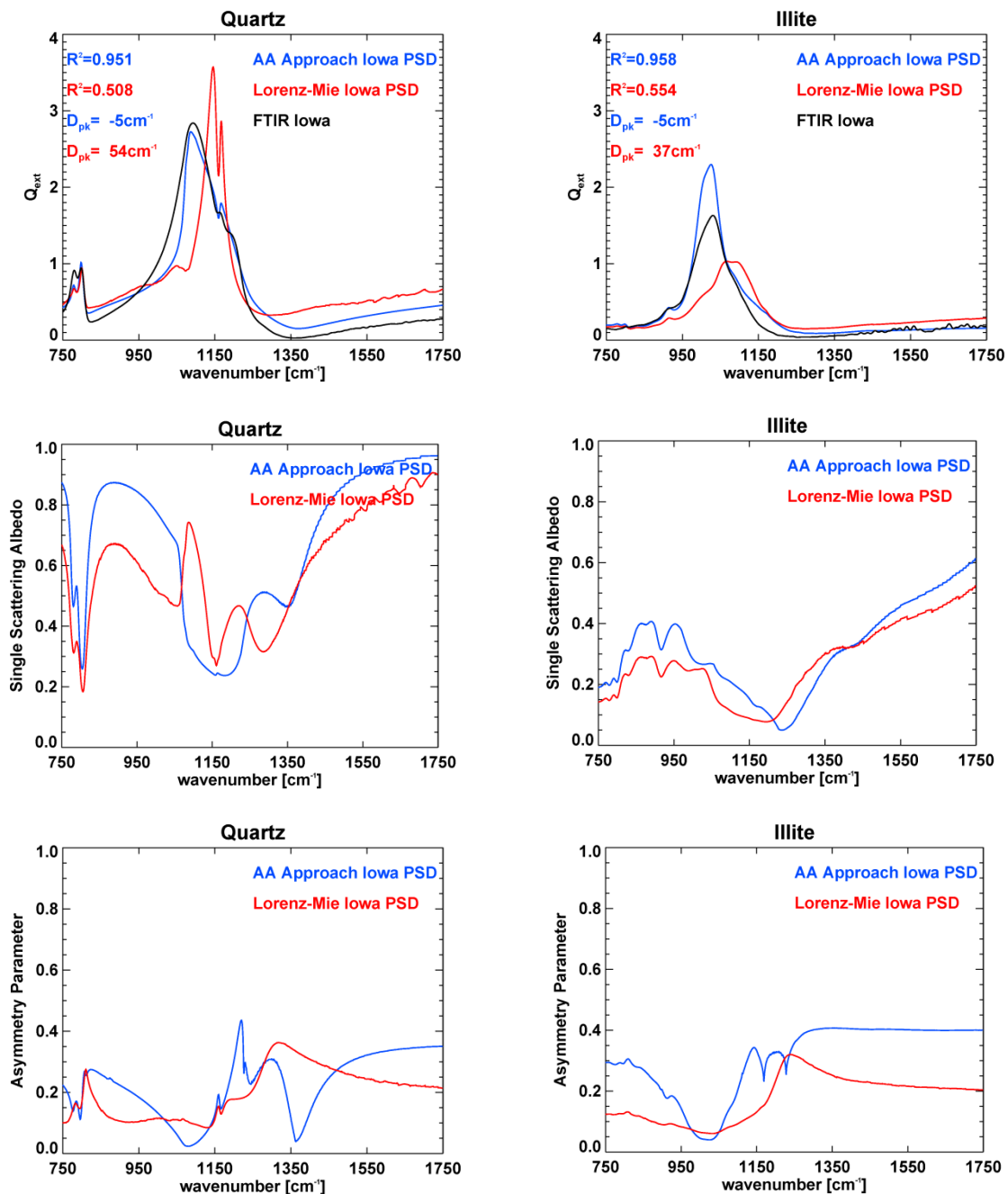


Figure 4.4-1: Extinction efficiency (top), single scattering albedo (middle) and asymmetry parameter (bottom) for quartz (left) and illite (right) as simulated with the AAA method (blue) and Lorenz-Mie theory (red) as well as corresponding laboratory measurements of the University of Iowa (black) in the terrestrial IR spectral region. The spectra and size distributions correspond to the measurements described in [RD14].

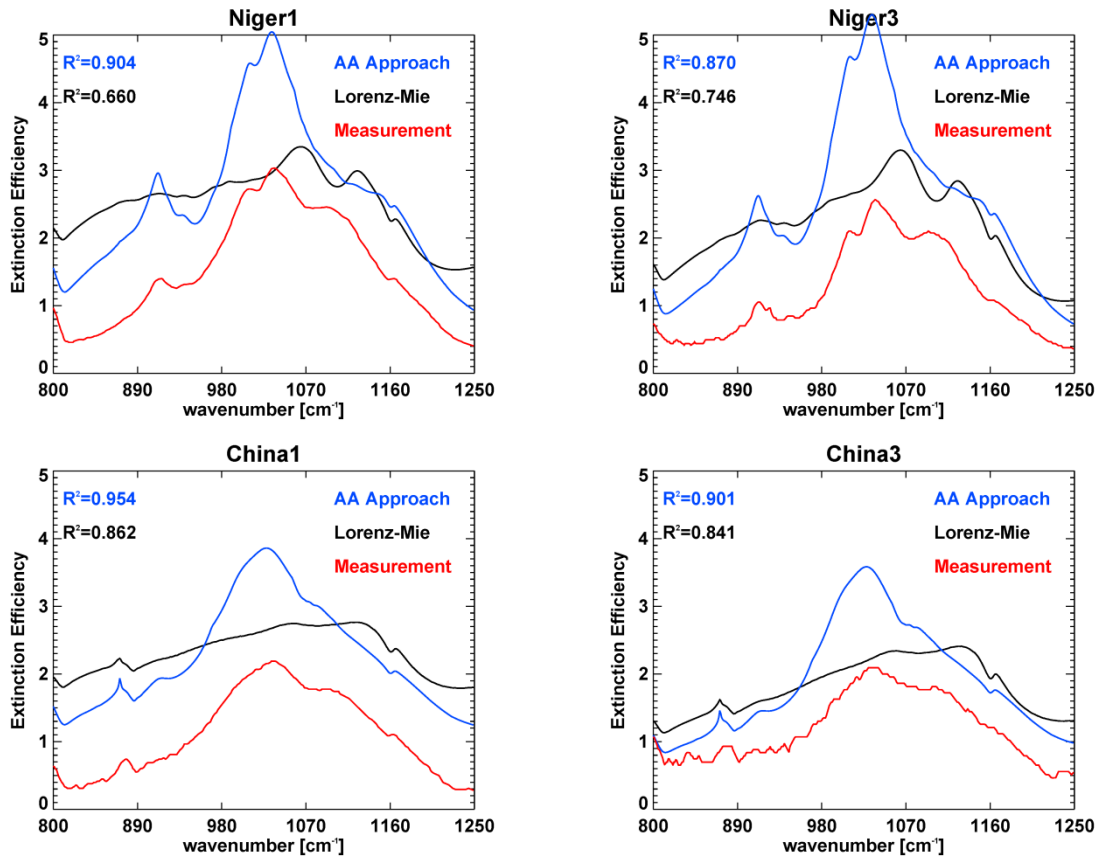


Figure 4.4-2: Extinction efficiency spectra of kaolinite rich (top) and illite and quartz rich (bottom) dust samples as simulated with the AAA method (blue) and Lorenz-Mie theory (black) as well as corresponding laboratory measurements of the University of Paris East (red) in the terrestrial IR window region. The figures correspond to dust extinction directly after injection into the atmospheric simulation chamber (left) and after 50 minutes residence time (right) and consequently to different size distributions as larger particles deposit faster (see [RD41]).

4.5 Theoretical considerations of the IMARS retrieval approach

The mathematical approach of IMARS v5.2 is based on forward simulations of various dust realizations and storage of the resulting scaled brightness temperature differences (see 4.2) in look-up tables (LUTs). The realizations include varying dust particle size distributions and mineralogical compositions as outlined above and also 5 different dust layer altitudes, expressed in the radiance ratio of blackbody emission characterized by the dust layer temperature and the surface temperature, as well as varying dust TIR AOD. Although it depends on the surface temperature, the altitude range covered by the approach is typically between 500m and 6km. The AOD range (TIR) covered varies between 0.01 and 3. The forward simulations are performed with the Two-Stream solution (eq.(2)) using AAA optical properties as outlined above and described in detail in [RD41], examples for ocean and desert surface emissivities and for different thermal contrasts between dust layer and surface are presented in Figure 4.5-1.

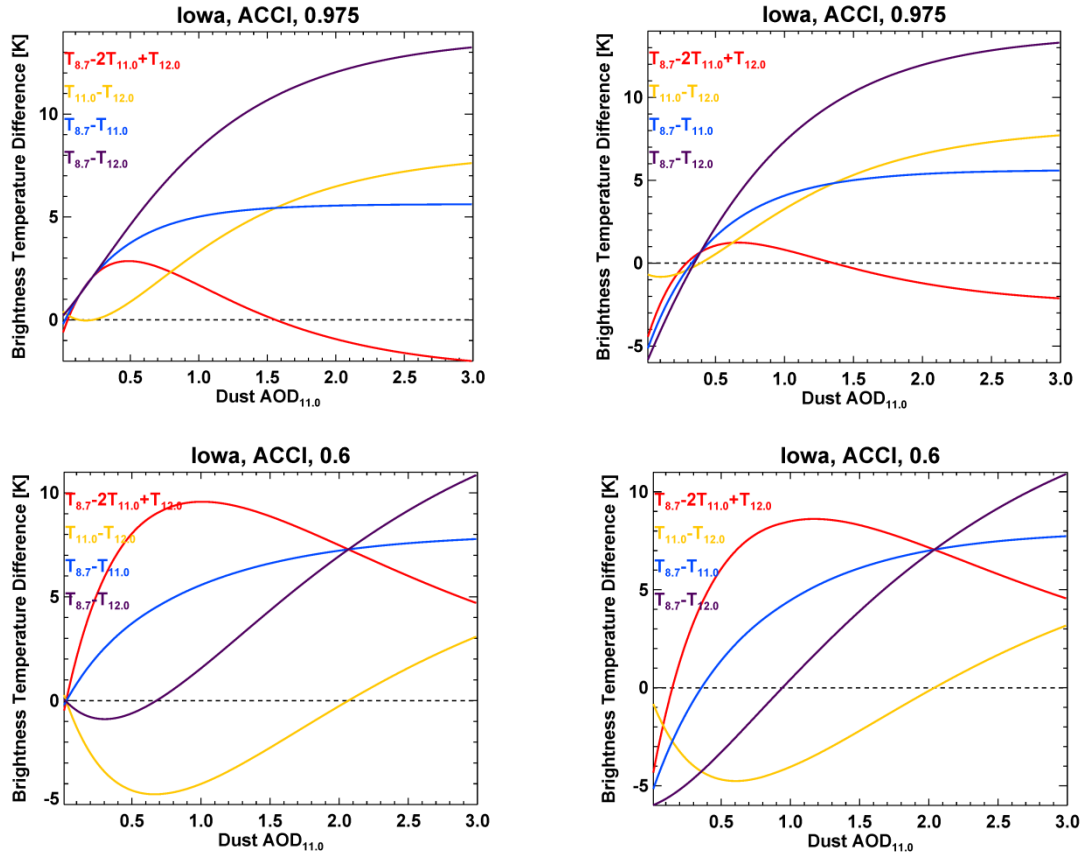


Figure 4.5-1: Example of simulated brightness temperature differences for various TIR AODs. These simulations have been performed with the “Iowa Loess” mixture and the lognormal “Aerosol_cci” particle size distribution for ocean (left) and desert (right) surface emissivities and for near-surface dust (approx. 500m, top) and an elevated dust layer (approx. 5km, bottom).

Based on these pre-tabulated look-up tables the IMARS retrieval generates a probability density function (PDF) over the full space of dust realizations. For each fixed dust particle size (index s), dust composition (index c) and dust layer height (index h) a partial probability for each AOD from each BTD is generated with a Gaussian metric:

$$P_i(s, c, h, \tau) = \exp \left[-0.5 \left(\frac{\widehat{BTD}_i(s, c, h, \tau) - BTD_i}{\sigma_i(s, c, h)} \right)^2 \right] \quad (46)$$

Here the subscript i denotes the index of the brightness temperature difference, BTD_i is the observed brightness temperature difference, \widehat{BTD}_i is the simulated brightness temperature difference and σ_i is the assumed noise level in BTD_i . In IMARS the noise level is set to 10% of the largest signal (i.e. BTD with the highest AOD) for all four brightness temperature differences.

It is assumed in the IMARS retrieval that the information conveyed by the four brightness temperatures are all independent from each other, although only three

	aerosol_cci IMARS ATBD	REF : IMARS-ATBD ISSUE : 2.0 DATE : 12.12.2016 PAGE : 24
---	---	---

channels are used as input. This assumption can be made because brightness temperature differences are used and not brightness temperatures, and because three out of four BTD express the differences between two channels whereas one contains information of all three bands. Indeed BTD_1 can be regarded as “brightness temperature difference difference, as $BTD_1 = BTD_3 - BTD_2$. If independence is assumed for all BTD_i , the LUT probability for each $\{s, c, h, \tau\}$ is

$$P(s, c, h, \tau) = \prod_{i=1}^4 P_i(s, c, h, \tau) \quad (47)$$

following the conventional rules for probability calculus. IMARS creates a PDF over the set $\{s, c, h\}$, thus the probability has to be aggregated over τ and an AOD value has to be assigned. This is done by averaging weighted with the corresponding τ -probability:

$$P(s, c, h) = \frac{\sum_j (P(s, c, h, \tau_j))^2}{\sum_j P(s, c, h, \tau_j)} \quad (48)$$

$$\tau^*(s, c, h) = \frac{\sum_j (P(s, c, h, \tau_j) \cdot \tau_j)}{\sum_j P(s, c, h, \tau_j)} \quad (49)$$

The overall dust probability P_{dust} is calculated from $\{P(s, c, h)\}_{s, c, h}$ analogous to eq. (43), the uncertainty of the dust retrieval (ε_{dust}) is estimated from the standard deviation of $\{P(s, c, h)\}_{s, c, h}$. After normalization, the [4x3x5] set $P(s, c, h)$ describes the PDF over size, composition and altitude of the observed dust with TIR AOD τ^* . The finally retrieved dust properties are then acquired by summation along the corresponding dimension(s):

$$R_{eff} = \sum_c \sum_s P(s, c) \cdot \widehat{R_{eff}}(s, c) \quad (50)$$

$$D_{mw} = \sum_c \sum_s P(s, c) \cdot \widehat{D_{mw}}(s, c) \quad (51)$$

$$T_{dust}(h) = \sum_h P(h) \cdot \widehat{T_{dust}}(h) \quad (52)$$

$$\gamma = \sum_s \sum_c \sum_h P(h) \cdot \tau^*(s, c, h) \quad (53)$$

$$AOD_{TIR} = \sum_s \sum_c \sum_h P(h) \cdot \tau^*(s, c, h) \quad (54)$$

$$AOD_{0.55\mu m} = \gamma \cdot AOD_{TIR} \quad (55)$$

where γ denotes the composition- and size-dependent ratio between TIR and visible (0.55 μ m) AOD. The dust mass column is estimated by calculating an infrared mass extinction efficiency ($= \frac{4\rho_{dust}R_{eff}}{3Q_e}$, where ρ_{dust} is the density of dust aerosol) based on composition and particle size analogous to eq. (45)-(47) and then multiplying AOD_{TIR} and the infrared mass extinction efficiency (see [RD40]). The density of quartz, thus 2.65 g/m³ has been used as ρ_{dust} for mass column calculation, as the densities of other silicates do not vary much from this value.

Using the concept of channel capacity ([RD57]), the number of individual variables distinguishable for each FOV (n_{var}) can be calculated from P_{dust} and ε_{dust} as

$$n_{var} = \sqrt{3} \log_2 \left(\frac{P_{dust} + \varepsilon_{dust}}{\varepsilon_{dust}} \right) \quad (56)$$

assuming the input capacity to be $\sqrt{3}$ (from 3 channels).

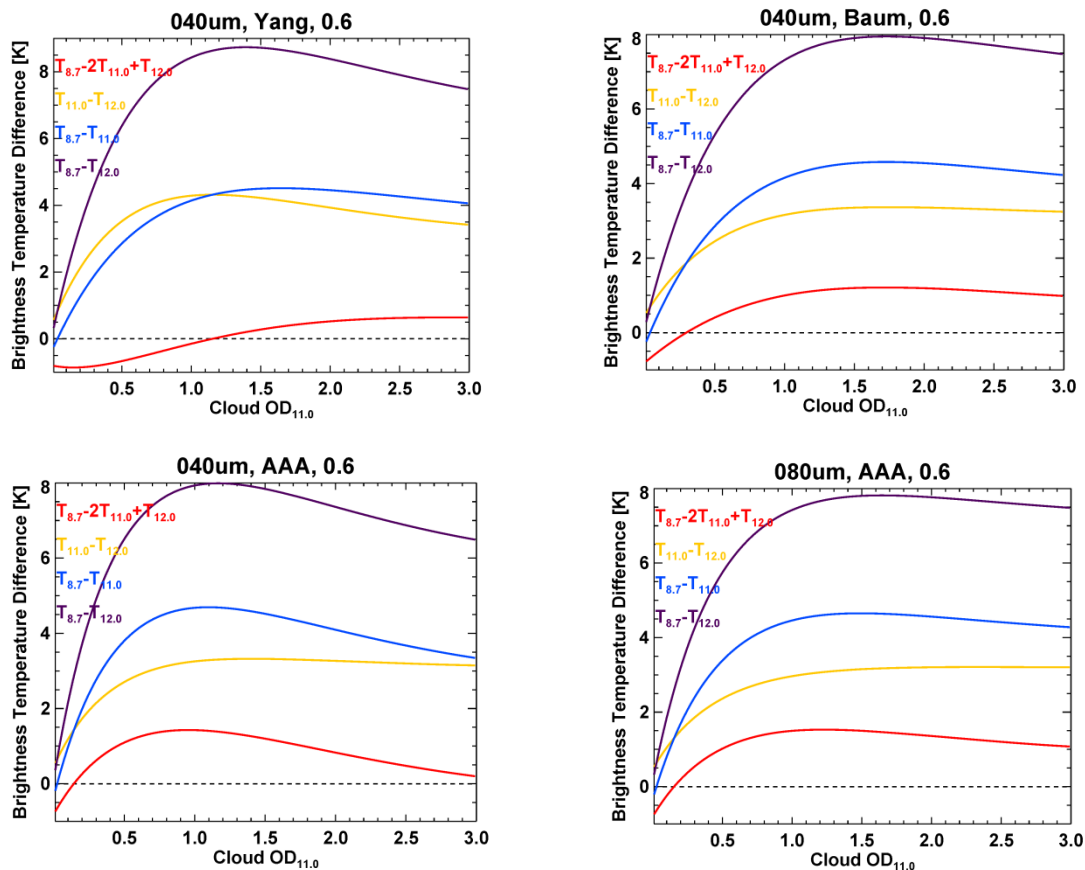


Figure 4.5-2: Example of simulated brightness temperature differences for various TIR ice cloud optical depths. These simulations have been performed for ocean surface emissivities at a moderate cloud height of (approx. 5km, bottom). Brightness temperature differences have been simulated for ice cloud with an effective diameter of $40\mu\text{m}$ with the parameterizations of *Yang et al. 2005* (top left), *Baum et al. 2013* (top right), and the AAA disk model (bottom left). For the latter also the impact of crystal size of the BTD is exemplarily presented for simulations with an effective radius of $80\mu\text{m}$.

An ice cloud retrieval is performed in exactly the same way. The ice cloud optical properties are calculated for four effective radius values of $\{10\mu\text{m}, 40\mu\text{m}, 80\mu\text{m}, 100\mu\text{m}\}$ and with three different parameterizations assuming different shape models. The parameterizations are the *Yang et al. 2005* model ([RD38]), the *Baum et al. 2013* model ([RD39]) and the AAA *disk* model.

For all variables like probability, uncertainty, optical depth, emission temperature etc. two values are available in IMARS: one for dust and one for (ice) clouds. The probabilities of dust and cloud feed into another derived variable: the *retrieval entropy* H . This quantity, introduced by [RD34] and further analyzed in [RD35], is often also referred to as *information content* or *Shannon information content*. In the case of IMARS the retrieval entropy is defined similarly to the information spectrum (eq. (9)) as

	aerosol_cci IMARS ATBD	REF : IMARS-ATBD ISSUE : 2.0 DATE : 12.12.2016 PAGE : 26
---	---	---

$$H = -(P_{dust} \cdot \log_2(P_{dust}) + P_{cloud} \cdot \log_2(P_{cloud})) \quad (57)$$

It describes the distinguishability between dust and cloud and thus the reliability of the *a posteriori* discrimination. The lower H , the more reliable the discrimination (toward either end). High H (typically somewhere around 1) indicates a non-reliable discrimination and the retrieval results should be used with great caution. Reasons for high H can be low optical depths (and thus an atmosphere containing neither significant amounts of dust nor ice cloud) or a spectral signal outside of the definitions of IMARS, for example due to surface emissivity or dominant gas absorption which is not considered. H is also internally used for probabilistic enhancement of the dust and cloud probabilities by

$$P_{dust|post} = P_{dust|prior} \cdot (1 - H \cdot P_{cloud|prior}) \quad (58)$$

$$P_{cloud|post} = P_{cloud|prior} \cdot (1 - H \cdot P_{dust|prior}) \quad (59)$$

Multiplication of the prior adverse probability and H yields enhancement of the posteriori probability in the case of weak discrimination between dust and clouds and has very little impact if both are well distinguished.

5 IMPLEMENTATION

5.1 IMARS processing environment

The IMARS processing environment consists of a core program implemented in FORTRAN (typically referred to as “IMARS”), a couple of preprocessors implemented in IDL (for extracting the required information from IASI L1C spectra in native file format and for generation of look-up tables and optical properties) and a postprocessor, also implemented in IDL (for casting the generic IMARS output to the exact file format specified for aerosol_cci and for producing output at higher data levels - Level-3 for example).

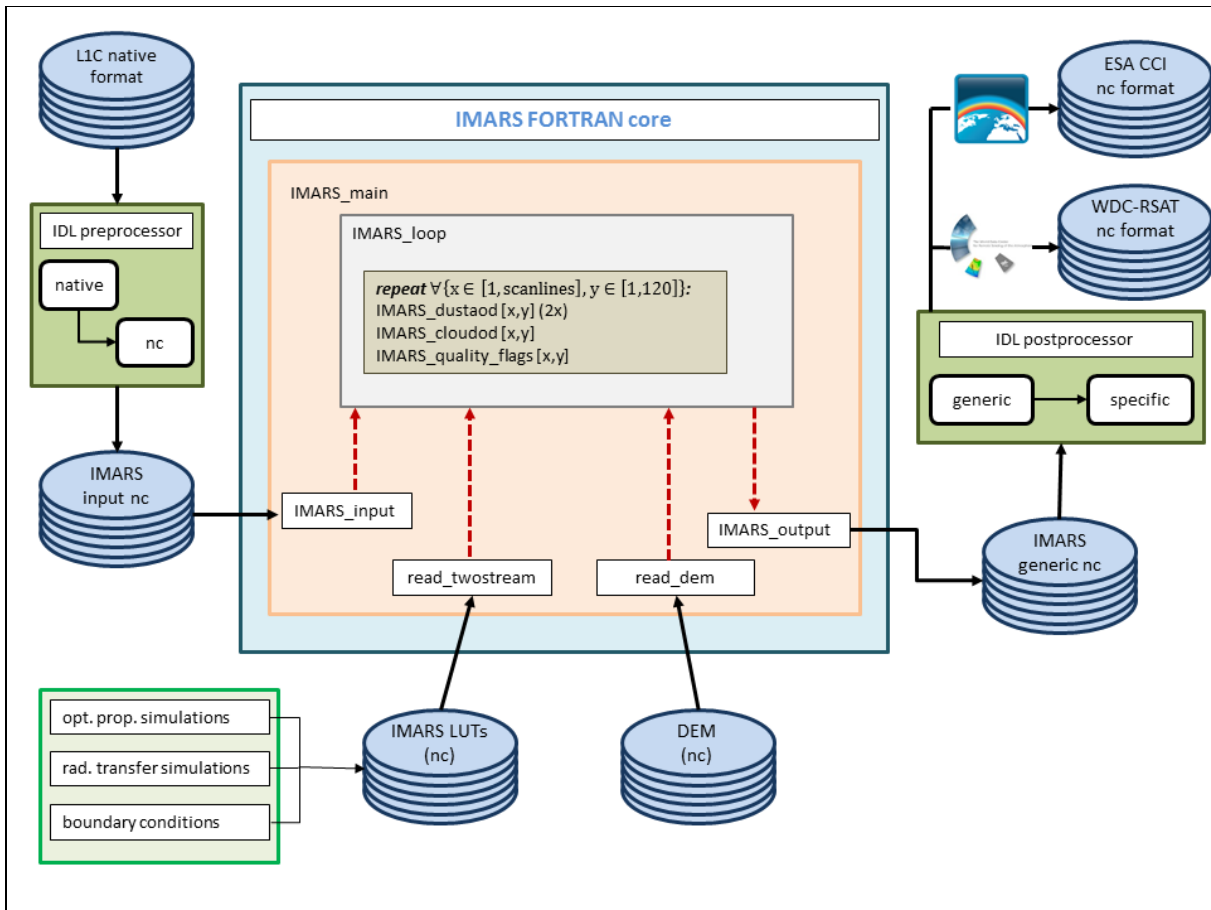


Figure 5.1-1: Overview of the IMARS processing environment.

	aerosol_cci IMARS ATBD	REF : IMARS-ATBD ISSUE : 2.0 DATE : 12.12.2016 PAGE : 28
---	---	---

5.2 Preparatory steps

From offline Two-Stream simulations lookup tables are pretabulated as described above. These steps are performed for dust simulations as well as for cirrus and each for ocean, (assumed to be very similar to vegetation, as both have low spectral contrast) and desert surface emissivities (see 5.3).

IASI Level 1 full resolution spectra provided from EUMETSAT are used to generate the input needed by IMARS (see section 6.1).

IASI radiance observations are collected into 28 bins represented by the maximum brightness temperature as described above. The bin collection is executed as preprocessor, as it is not necessary to repeat this time consuming step for each algorithm update.

The retrieval is run separately for each observed spectrum and thus can be applied in any granularity of the input data without constraints on spatial coverage. The first step is then to aggregate the bins into the four scaled brightness temperature differences needed for the retrieval.

5.3 Surface emissivity

Example surface emissivities for ocean and desert surfaces have been compiled from the MODIS UCSB Emissivity Library of the Institute for Computational Earth System Science (ICESS) at the University of California, Santa Barbara (UCSB). They can be accessed online at

<http://www.ices.ucsb.edu/modis/EMIS/html/em.html>

(as of October 12, 2014) and include spectra of water, ice and snow surfaces, soils and minerals as well as vegetation. As no prior land use atlas is applied, the retrieval is run twice over land, once with emissivities of vegetated surfaces (low spectral contrast, ocean emissivity is used as proxy) and once with desert emissivities (high spectral contrast). The results are weighted according to their relative dust probabilities. As ice clouds have inverse spectral behaviour the two-step approach is omitted for clouds, i.e. no specific cloud retrieval with desert emissivities is performed.

5.4 Implementation of the core dust retrieval

IMARS performs cloud screening *a posteriori*. There have been experiments with a priori cloud masks (thus the module "imars_cloudmask" in Figure 5.4-1), but these are not used for cloud detection in the IASI version of IMARS. IASI IMARS cloud detection is entirely based on the a posteriori quality and probability information provided by the retrieval itself. In terms of the retrieval methodology that means, that for every IASI FOV two retrieval chains (as described in 4.5) are run independently, one for dust and one for ice clouds. Only after full information about dust and clouds, specifically including probabilities and uncertainties, are available these are used for quality assessment of both retrieval branches and finally for the decision whether the FOV is more likely to contain dust or cloud or none of both (rejection of both branches due to low quality).

Generation of quality flags and cloud filtering are described below in sections 5.5 and 5.6, respectively. The IMARS core algorithmic chain is depicted schematically in Figure 5.4-1.

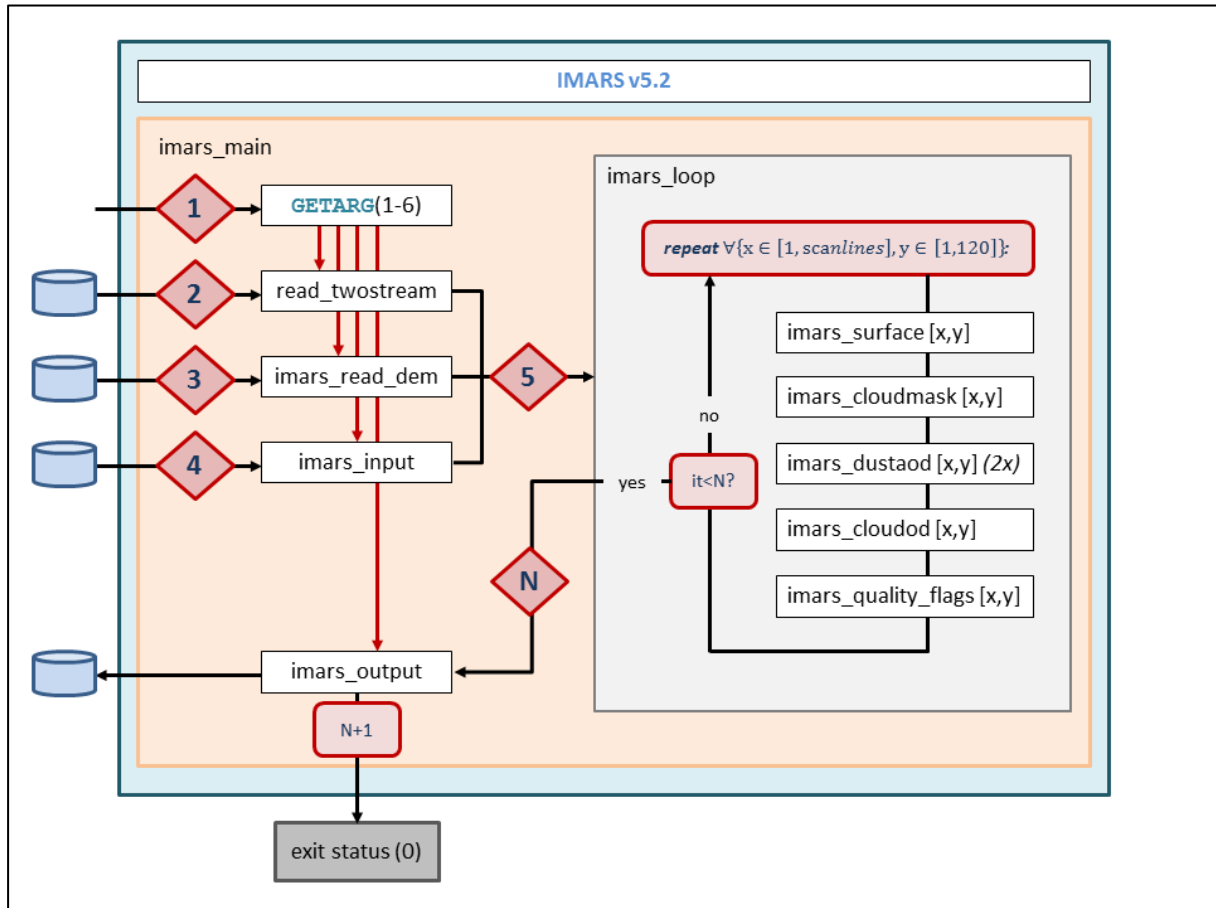


Figure 5.4-1: Program flow chart of the IMARS retrieval. The retrieval loop is repeated for all FOVs per scanline and for all scanlines of the granule/orbit. This flow chart is a close-up of the blue box in Figure 5.1-1.

Figure 5.4-2 depicts the more algorithmic design of the retrieval flow per FOV. Starting from the observations, the four scaled brightness temperature differences are used as input independently for the dust and the ice cloud retrieval chain. Only after both return results (which always have optical depth > 0 by design), their quality is assessed by generating independent quality flags for dust and ice clouds and by calculating the retrieval entropy (eq. (57)). After all information (physical, probabilistic and quality) is available, the assessment if the FOV contains most likely dust or ice cloud or none is performed.

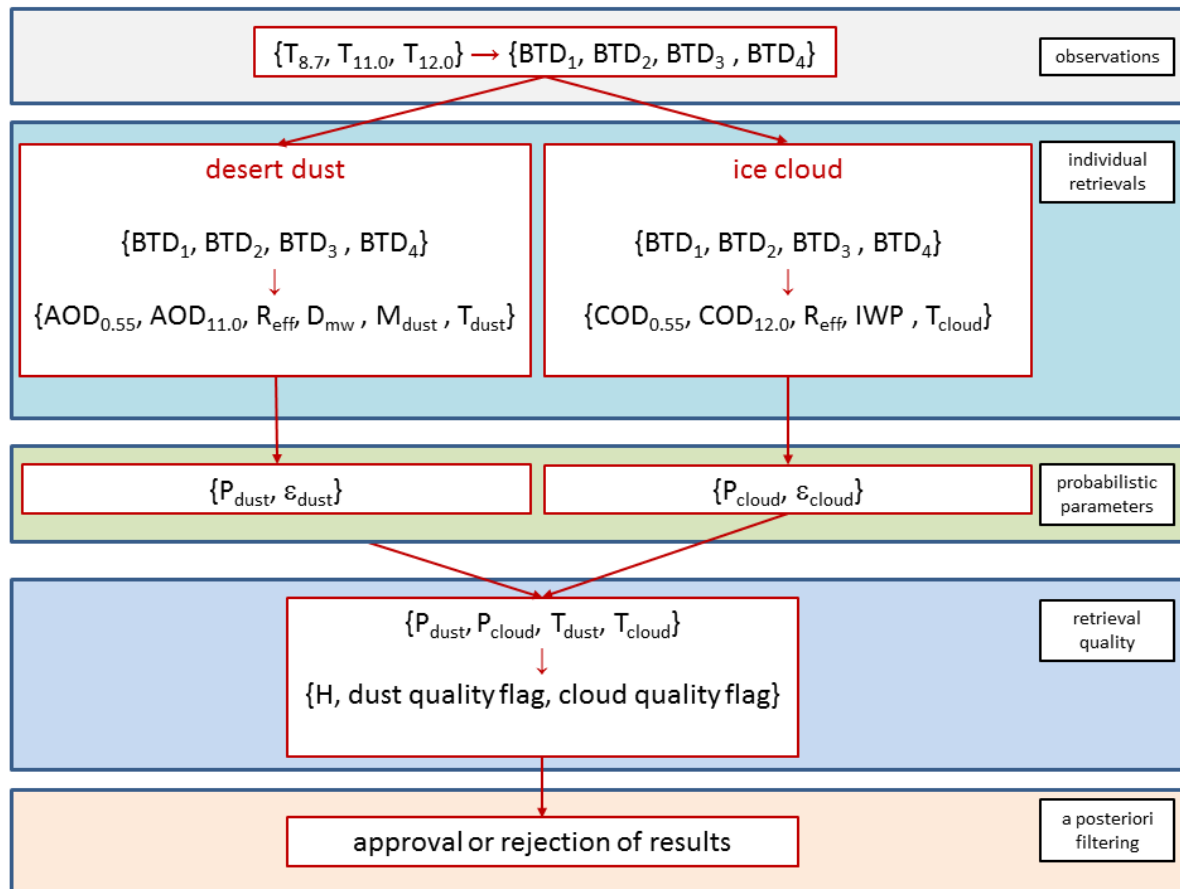


Figure 5.4-2: Modular design of the IMARS version 5.2 algorithm chain, independently performed for each FOV. This module plot is a schematic close-up of the white box (“imars_loop”) in Figure 5.4-1.

5.5 Quality Flags

Quality flags are derived for mineral dust and ice cloud observations separately based on the same physical principles. In general an observation is assumed to be reliable, if the intrinsic uncertainty ε is small, the probability estimate is high and the emission temperature is lower than the surface temperature (as approximated by T_{base}) and within an expected range (cold for ice clouds, rather warm for desert dust). Moreover the comparison of quality indicators for dust and clouds is used for assessing the possibility of contamination by the respectively other variable. The conditions for quality flag increase are presented in Table 5.5-1. Each time a condition is fulfilled by the observations, the value of the quality flag (QF) is increased by 1. Consequently a QF value of 0 indicates absolutely unreliable conditions (generally no values are retrieved at all) and QF=10 indicates perfect conditions with the highest level of reliability (see also Table 8.1-1). Quality flags for desert dust (DQF) and ice clouds (CQF) are formulated exactly analogously, as also the retrieval blocks follow exact the same mathematics.

	aerosol_cci IMARS ATBD	REF : IMARS-ATBD ISSUE : 2.0 DATE : 12.12.2016 PAGE : 31
---	---	---

Consequently the resulting quality flags for dust and cloud are fully comparable and rely on the same intrinsic quality measures.

Table 5.4-1: Quality flag conditions in IMARS

Conditions for increasing mineral dust QF	Conditions for increasing ice cloud QF
$P_{dust} > 0.25$ and $P_{cloud} < 0.75$	$P_{cloud} > 0.25$ and $P_{dust} < 0.75$
$P_{dust} > 0.5$ and $P_{cloud} < 0.5$	$P_{cloud} > 0.5$ and $P_{dust} < 0.5$
$P_{dust} > 0.75$ and $P_{cloud} < 0.25$	$P_{cloud} > 0.75$ and $P_{dust} < 0.25$
$\epsilon_{dust} < 0.5$ and $P_{dust} > 0.25$ and $T_{dust} > 240K$	$\epsilon_{cloud} < 0.5$ and $P_{cloud} > 0.25$ and $T_{cloud} < 270K$
$\epsilon_{dust} < 0.3$ and $P_{dust} > 0.5$ and $T_{dust} > 240K$	$\epsilon_{cloud} < 0.3$ and $P_{cloud} > 0.5$ and $T_{cloud} < 270K$
$\epsilon_{dust} < 0.5$ and $N_{var}(dust) > N_{var}(cloud)$ and $T_{dust} > 240K$	$\epsilon_{cloud} < 0.5$ and $N_{var}(cloud) > N_{var}(dust)$ and $T_{cloud} < 270K$
$\epsilon_{dust} < 0.3$ and $N_{var}(dust) > N_{var}(cloud)$ and $T_{dust} > 240K$	$\epsilon_{cloud} < 0.3$ and $N_{var}(cloud) > N_{var}(dust)$ and $T_{cloud} < 270K$
$P_{dust} > P_{cloud}$ and $N_{var}(dust) > N_{var}(cloud)$ and $N_{var}(dust) > 3$	$P_{cloud} > P_{dust}$ and $N_{var}(cloud) > N_{var}(dust)$ and $N_{var}(cloud) > 3$
$\epsilon_{dust} < 0.5$ and $P_{dust} > P_{cloud}$ and $N_{var}(dust) > N_{var}(cloud)$ and $T_{dust} > 280K$	$\epsilon_{cloud} < 0.5$ and $P_{cloud} > P_{dust}$ and $N_{var}(cloud) > N_{var}(dust)$ and $T_{cloud} < 270K$
$\epsilon_{dust} < 0.3$ and $P_{dust} > P_{cloud}$ and $N_{var}(dust) > N_{var}(cloud)$ and $T_{dust} > 260K$	$\epsilon_{cloud} < 0.3$ and $P_{cloud} > P_{dust}$ and $N_{var}(cloud) > N_{var}(dust)$ and $T_{cloud} < 250K$

5.6 A posteriori cloud discrimination and approval of results

Cloud screening is performed *a posteriori* based on the retrieval results. Basically it is done by comparing the number of independent variables and quality flags for dust and clouds, partially bound by retrieved optical depth (AOD or COD) and probabilities. The cloud discrimination tests listed in Table 5.5-1 are performed in consecutive order, the final test just states that if none of the prior tests is passed, the observation is designated neither dust nor cloud (so none of them is a default or preferred decision).

Table 5.5-1: Quality flag conditions in IMARS

Test No.	Test conditions	Decision
1	($AOD > 0$ and $DQF > 1$ and $N_{var}(dust) > N_{var}(cloud)$)	"dust"
2	($COD > 0$ and $CQF > 1$ and $N_{var}(cloud) > N_{var}(dust)$)	"cloud"
3	(<i>None of above</i> and $AOD > 0.05$ and $DQF > 1$ and $P_{dust} > P_{cloud}$)	"dust"
4	(<i>None of above</i> and $COD > 0.2$ and $CQF > 1$ and $P_{cloud} > P_{dust}$)	"cloud"
5	(<i>None of above</i> and $AOD > 0$ and $DQF > 2$)	"dust"
	(<i>None of above</i>)	"none"

	aerosol_cci IMARS ATBD	REF : IMARS-ATBD ISSUE : 2.0 DATE : 12.12.2016 PAGE : 32
---	---	---

This approach guarantees that each observation is designated as either representing dust or ice cloud or none of them. No observation can contain information on both dust and clouds and thus no contradicting results are provided by the IMARS desert dust and ice cloud retrieval. As dust and cloud discrimination is based on the passing of positive tests and not on decisions including negative tests, every decision results from a sufficient belief in the reliability of the results rather than the exclusion of the contradictory. Such a positive-test decision tree is consequently a part of quality assurance by itself.

5.7 Retrieval examples

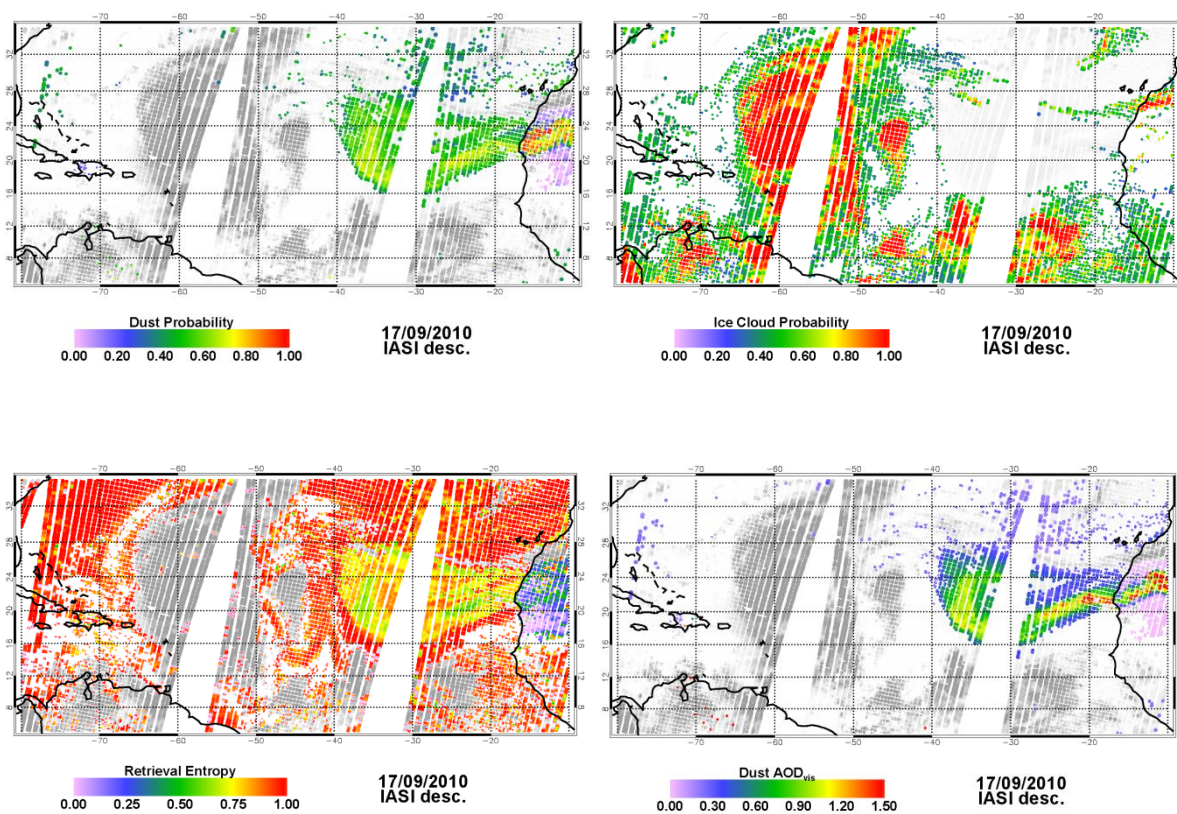


Figure 5.6-1: IMARS results for P_{dust} (top left) and P_{cloud} (top right) and H (bottom left) as well as dust $AOD_{0.55\mu m}$ (bottom right) for the large dust outbreak off the coast of West Africa on 17 September 2010 observed with IASI on board Metop-A.

A strong large-scale dust outbreak from the West Sahara to the Atlantic Ocean is shown in terms of IMARS retrieval results in Figure 5.7-1. The figure shows dust and ice cloud probabilities as examples, indicating the confidence in the positions of the dust plume and deep convective clouds. Moreover the retrieval entropy H (Shannon information content) and dust $AOD_{0.55\mu m}$ are presented. Dust properties (P_{dust} , $AOD_{0.55\mu m}$) are depicted

only for FOVs identified as containing dust as described in 5.5 and P_{cloud} is shown for cloudy observations only. Grey IASI FOVs scale with T_{base} in such way that cold observations appear dark grey whereas light grey indicates warm baseline temperatures. Greyscale is applied in the case of no successful retrieval available. It is clearly evident that also H conveys very useful information for the interpretation of the retrieval results and thus additional valuable quality information. In the case of the deep convective cloud cores (especially the two hurricanes in the Western part of the plot) P_{dust} is so low that H becomes mathematically unstable and thus is reported as missing information (greyscale areas in H plot). For the dust plume it can be seen that the value of H is low where it is obvious that the observation is dust and not cloud (e.g. over the high dust AOD areas and over the Sahara desert). Other regions, characterized by high H , represent observations where not much trust should be granted to the discrimination between dust and clouds. This is not necessarily connected to low optical depths returned by the retrieval (e.g. over continental South America). A more detailed discussion on guidelines for using the quality information in IMARS can be found in chapter 8.

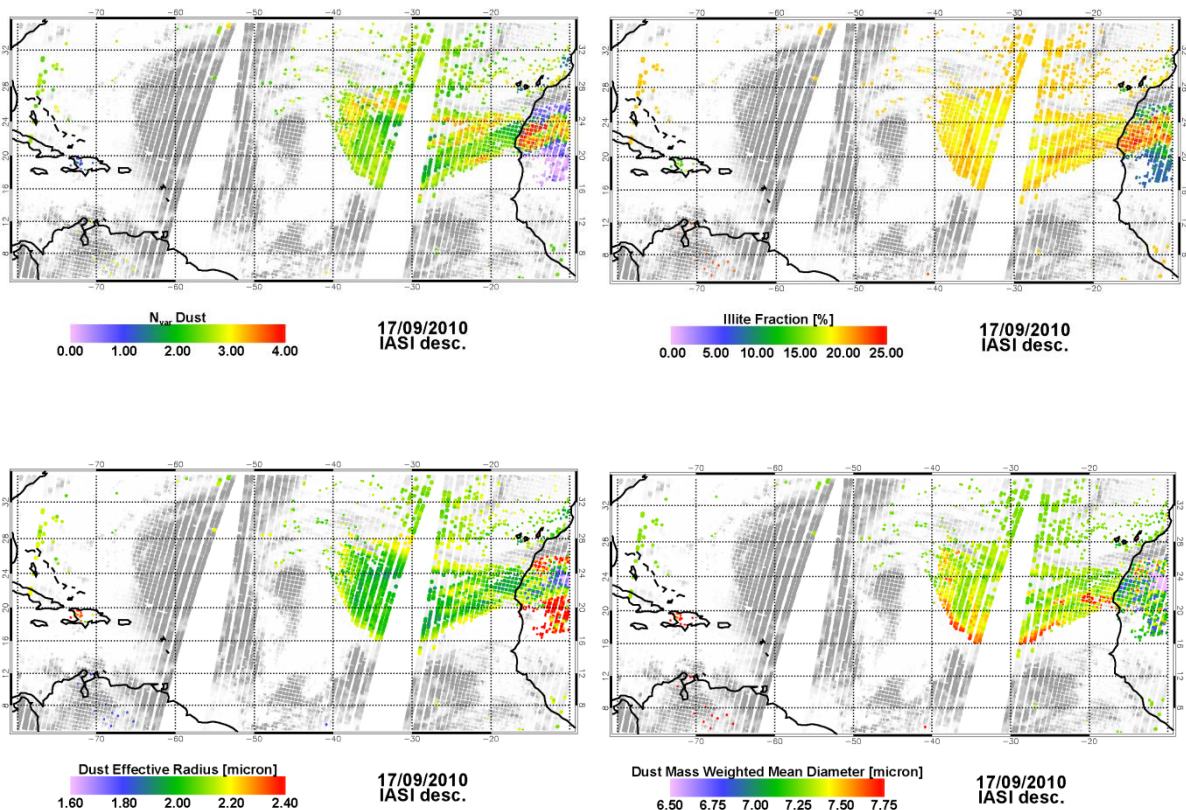


Figure 5.6-2: IMARS results for dust N_{var} (top left) and illite abundance (top right) as well as the two size distribution representations R_{eff} (bottom left) and D_{mw} (bottom right) for the large dust outbreak off the coast of West Africa on 17 September 2010 observed with IASI on board Metop-A.

	aerosol_cci IMARS ATBD	REF : IMARS-ATBD ISSUE : 2.0 DATE : 12.12.2016 PAGE : 34
---	---	---

Figure 5.7-2 complements the dust plume information of this day by depicting the number of independent dust variables, the illite abundance in the plume as well as the characterization of the particle size distribution in terms of effective radius and mass-weighted diameter. The typical number of independently distinguishable dust variables in the plume is between 2 and 3 over the ocean and reaches up to 4 over the desert (but here variable ε_{sfc} is contained in that number, too, as it effectively is retrieved as well!). In the low AOD area over land the number of independent variables drops significantly, also below 1, which means that even AOD is not well represented with sufficient reliability in the observations. The illite abundance shows a significant variability over the scene and indicates that the mineralogical composition might be used as plume tracer for dust source identification. Effective radius and mass-weighted diameter are not perfectly correlated, e.g. along the Southern edge of the plume over the ocean, although both represent dust particle size. Consequently the retrieval provides more than one piece of information about particle size and hints also to the size distribution.

Figure 5.7-3 shows selected IMARS dust retrieval results for a large dust sweep from the Taklimakan and Gobi deserts towards Korea, Japan and the Pacific Ocean on 21 March 2010. The masking effect of clouds above dust plumes become clearly evident from this example (e.g. along the Northern edges of the Taklimakan and Gobi deserts). The figure shows the set of dust quality assurance variables available from IMARS (probability, uncertainty, number of independent variables and the quality flag). Together with the retrieval entropy, these variables can be used (besides the guidelines to be presented in chapter 8) to apply any quality filter specifically tailored to the needs of the corresponding application, as a lot more quality information than a single binary "good/bad" flag is at disposal from IMARS. Furthermore in Figure 5.7-3 the $0.55\mu\text{m}$ dust AOD is depicted together with γ , the ratio between $0.55\mu\text{m}$ dust AOD and $10\mu\text{m}$ dust AOD. It can be seen that γ is highly variable within the IMARS retrieval as a result of the varying size distribution and dust composition information.

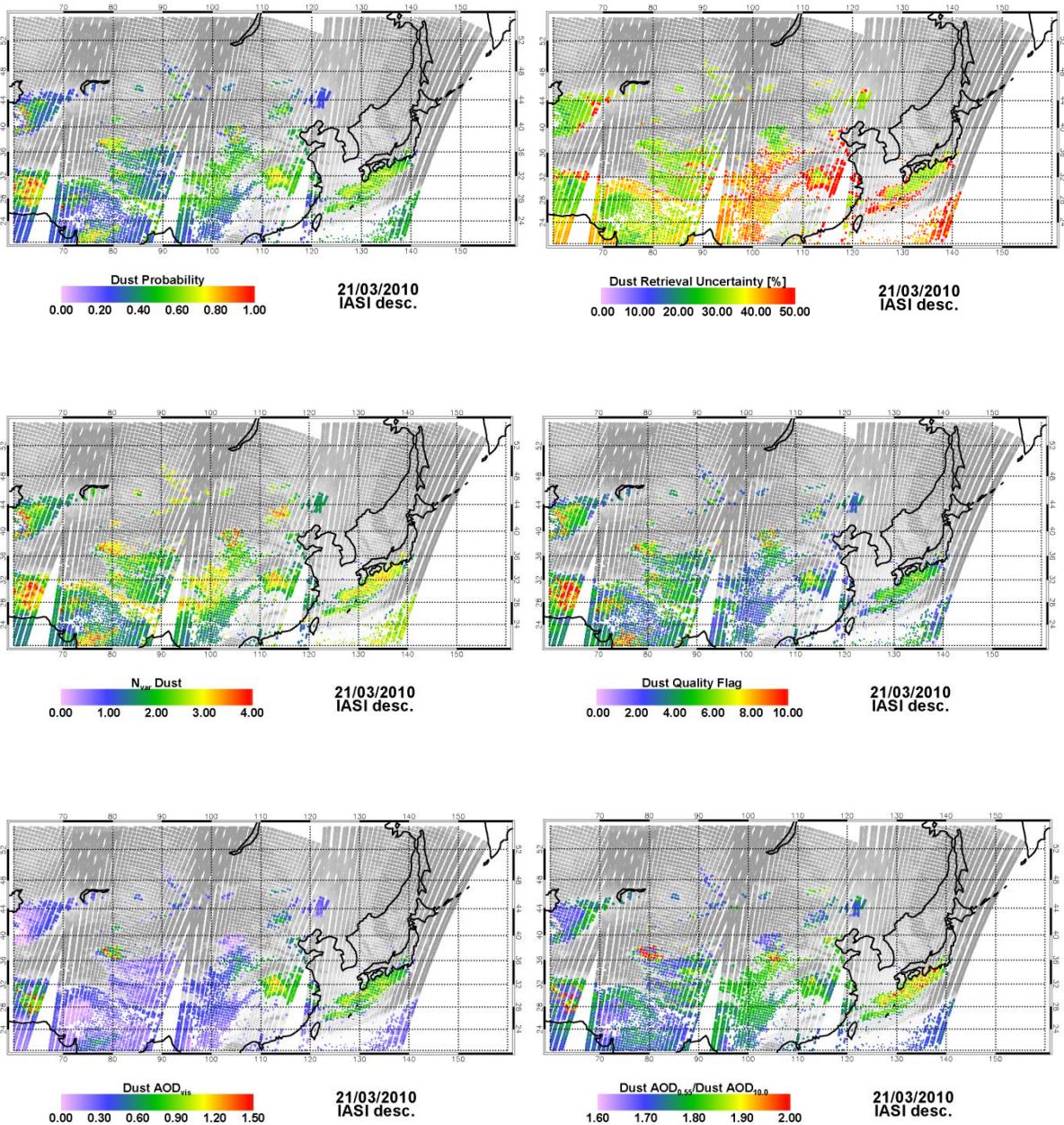


Figure 5.6-3: IMARS results for P_{dust} (top left), ϵ_{dust} (top right), dust N_{var} (middle left) dust quality flag (middle right), dust AOD_{0.55 μ m} (bottom left) and AOD ratio between 0.55 μ m and 10 μ m (bottom right) for a dust outbreak from the Asian deserts on 21 March 2010 observed with IASI on board Metop-A.

	aerosol_cci IMARS ATBD	REF : IMARS-ATBD ISSUE : 2.0 DATE : 12.12.2016 PAGE : 36
---	---	---

6 INPUT DATA REQUIREMENTS

6.1 IASI L1C data

The spectral input for IMARS is generated from IASI level 1C radiance files. These are acquired in the EUMETSAT native data format as full spectra (product code “_xxx_”, preferred version) or in the EUMETSAT Principal Component Scores product (product code “_pcs_”). Data have to be delivered with correct geolocation, viewing angle and observation time.

In order to facilitate the processing IMARS is designed to build on preprocessed data or spectral input from earlier IMARS versions. Accordingly the minimum requirement of input data is spectrally binned brightness temperatures or radiances in the $833\text{cm}^{-1} - 1250\text{cm}^{-1}$ band as described above, at least containing the 35 bin values used for the retrieval (as specified in Table 7.1-1). The preprocessed data have to contain geolocation, viewing angles and observation time in the same array structure as the spectral input (Table 7.1-1). Consequently the input to IMARS v5.2 is not original EUMETSAT IASI L1C spectra but dedicated IMARS input files. Theoretically it is also possible to provide input from other sensors, as long as they are able to provide the three brightness temperatures used in IMARS. Unfortunately for narrowband instruments the spectral binning aiming at minimizing the gas absorption impact (especially from water vapour) is not available so that the quality will necessarily be reduced from imager input data.

6.2 Auxiliary data

The auxiliary data include the lookup tables for dust and ice cloud as described in chapter 4. IMARS moreover requires surface elevations. Currently the ETOPO-2 digital elevation model (DEM) is used for mapping surface elevation onto a global 0.1° latitude/longitude grid.

Table 6.2-1 compiles the required input of auxiliary data as currently implemented in IMARS together with the corresponding sources of the data. For sources only the last instance of source has been presented. While these can themselves rely on auxiliary inputs, for example refractive indices in the case of AAA simulations or optical properties in the case of the Two-Stream simulations, these details can be found in the above chapters of this document and are moreover not essential for the IMARS algorithm. For example does IMARS only require dust optical properties. The algorithm does not require them being derived from AAA simulations, other methods would also be possible (e.g. T-Matrix for optical properties, advanced radiative transfer modelling instead of the Two-Stream approximation for the lookup tables).



Table 6.2-1: Required auxiliary datasets for IMARS and corresponding currently used sources.

Auxiliary dataset	Dimensions	Source	Data format
Digital elevation model	7200x3600	ETOPO-2 on 0.1° lat/lon projection	netCDF-3
Dust R_{eff}	4x6	Table 4.3-1	netCDF-4
Dust D_{mw}	4x6	Table 4.3-2	netCDF-4
Dust composition matrix	4x6	Table 4.3-3	netCDF-4
Dust g (TIR)	3x4	AAA	netCDF-4
Dust ω_0 (TIR)	3x4	AAA	netCDF-4
Dust γ	3x4	AAA	netCDF-4
Dust Q_e (TIR)	3x4	AAA	netCDF-4
Dust BTD_1 LUT ocean surface	100x5x3x4	AAA/Two-Stream	netCDF-4
Dust BTD_2 LUT ocean surface	100x5x3x4	AAA/Two-Stream	netCDF-4
Dust BTD_3 LUT ocean surface	100x5x3x4	AAA/Two-Stream	netCDF-4
Dust BTD_4 LUT ocean surface	100x5x3x4	AAA/Two-Stream	netCDF-4
Dust BTD_1 LUT desert surface	100x5x3x4	AAA/Two-Stream	netCDF-4
Dust BTD_2 LUT desert surface	100x5x3x4	AAA/Two-Stream	netCDF-4
Dust BTD_3 LUT desert surface	100x5x3x4	AAA/Two-Stream	netCDF-4
Dust BTD_4 LUT desert surface	100x5x3x4	AAA/Two-Stream	netCDF-4
Cloud R_{eff}	4	intrinsic	netCDF-4
Cloud g (TIR)	3x4	literature+AAA	netCDF-4
Cloud ω_0 (TIR)	3x4	literature+AAA	netCDF-4
Cloud γ	3x4	literature+AAA	netCDF-4
Cloud Q_e (TIR)	3x4	literature+AAA	netCDF-4
Cloud BTD_1 LUT ocean surface	100x5x3x4	literature+AAA/Two-Stream	netCDF-4
Cloud BTD_2 LUT ocean surface	100x5x3x4	literature+AAA/Two-Stream	netCDF-4
Cloud BTD_3 LUT ocean surface	100x5x3x4	literature+AAA/Two-Stream	netCDF-4
Cloud BTD_4 LUT ocean surface	100x5x3x4	literature+AAA/Two-Stream	netCDF-4
Cloud BTD_1 LUT desert surface	100x5x3x4	literature+AAA/Two-Stream	netCDF-4
Cloud BTD_2 LUT desert surface	100x5x3x4	literature+AAA/Two-Stream	netCDF-4
Cloud BTD_3 LUT desert surface	100x5x3x4	literature+AAA/Two-Stream	netCDF-4
Cloud BTD_4 LUT desert surface	100x5x3x4	literature+AAA/Two-Stream	netCDF-4
Altitude level radiance ratio	5	intrinsic	netCDF-4
TIR simulation optical depth	100	intrinsic	netCDF-4



7 ALGORITHM OUTPUT

7.1 Generic IMARS output

Table 7.1-1: Output datasets contained in the generic IMARS output.

Dataset name	Dim.	Type	Scale	Content
"lat"	SLx120	Flt32	1.0	Latitude of FOV center
"lon"	SLx120	Flt32	1.0	Longitude of FOV center
"VZA"	SLx120	Flt32	1.0	Viewing zenith angle for FOV center
"UTC"	SLx120	Flt32	1.0	UTC time of observation in dec. hours
"Elevation"	SLx120	Flt32	1.0	Average surface elevation of FOV
"Landmask"	SLx120	Int16	1	Landmask for IASI FOV
"Tbase"	SLx120	Int16	10	FOV Baseline temperature
"Entropy"	SLx120	Int16	10 ²	Retrieval entropy
"DQF"	SLx120	Int16	1	Dust quality flag
"DNIV"	SLx120	Int16	10 ²	Number of independent dust var.
"DAOD550"	SLx120	Int16	10 ³	Dust AOD at 0.55μm
"DAOD10"	SLx120	Int16	10 ³	Dust AOD at 10μm
"DAOD11"	SLx120	Int16	10 ³	Dust AOD at 11μm
"Dmass"	SLx120	Int16	10 ²	Dust mass column
"DReff"	SLx120	Int16	10 ²	Dust effective radius
"DMWMD"	SLx120	Int16	10 ²	Dust mass-weighted mean diameter
"DLT"	SLx120	Int16	10	Dust layer effective temperature
"DProbability"	SLx120	Int16	10 ³	Dust probability
"DUncertainty"	SLx120	Int16	10	Dust retrieval uncertainty
"DQuartzFraction"	SLx120	Int16	10 ³	Quartz abundance in dust
"DilliteFraction"	SLx120	Int16	10 ³	Illite abundance in dust
"DKaoliniteFraction"	SLx120	Int16	10 ³	Kaolinite abundance in dust
"DMontmorilloniteFraction"	SLx120	Int16	10 ³	Montmorillonite abundance in dust
"DFeldsparFraction"	SLx120	Int16	10 ³	Feldspar abundance in dust
"DCalciteFraction"	SLx120	Int16	10 ³	Calcite abundance in dust
"CQF"	SLx120	Int16	1	Cloud quality flag
"CNIV"	SLx120	Int16	10 ²	Number of independent cloud var.
"COD550"	SLx120	Int16	10 ³	COD at 0.55μm
"COD12"	SLx120	Int16	10 ³	COD at 12μm
"CWP"	SLx120	Int16	10 ²	(Ice) Cloud water path
"CReff"	SLx120	Int16	10 ²	(Ice) Cloud effective radius
"CTT"	SLx120	Int16	10	Cloud top temperature
"CProbability"	SLx120	Int16	10 ³	Cloud probability
"CUncertainty"	SLx120	Int16	10	Cloud retrieval uncertainty

The content of the generic IMARS output is compiled in Table 7.1-1. The table contains the dataset name in the output files, the dimensions ("Dim.") of the output as well as the data type ("Type") and, if applied, a scaling factor ("Scale"). The last column

	aerosol_cci IMARS ATBD	REF : IMARS-ATBD ISSUE : 2.0 DATE : 12.12.2016 PAGE : 39
---	---	---

describes the content of the dataset. In the IASI implementation of IMARS dimensions are fixed for anything but the number of scanlines (SL) which depends on the granularity of the IASI input format. Each IASI scanline contains 120 Fields-of-View, 30 views from 4 (2x2) detectors (see chapter 2 on instrument characteristics). Scaling factor is used for casting 32bit floating point variables to 16bit integer in order to save storage memory. Consequently the original value of the variable is obtained through dividing the stored output value by SF. No offset is used in the data type casting in IMARS. Although not all variables listed in Table 7.1-1 are casted into the Aerosol_cci IMARS netCDF files, the Table 7.1-1 is complete with regard to what is generally available (and thus can be provided upon request) from IMARS v5.2.

7.2 IMARS aerosol_cci specific output

In order to comply with the aerosol_cci data formats and naming convention the IMARS output contains a subset of the resulting variables of the IMARS algorithm while the generic output is stored in generic IMARS data format (netCDF-4 as well) and can be provided on request. The list of variables together with corresponding dataset names contained in the aerosol_cci IMARS output files is presented in Table 7.2-1. The dataset names follow the aerosol_cci naming convention, the data format of the aerosol_cci IMARS output complies with the aerosol_cci data standards and conventions as documented in the Product Specification Document (PSD, [AD3]). Table 7.2-1 is a specific subset of the general definitions made in the PSD. As IMARS is capable of retrieving more dust information that specified in the PSD (there, dust AOD at three wavelengths, effective radius and dust layer height are specified), Table 7.2-1 is extended by the names of those variables not covered by the PSD. These are basically probabilistic variables (dust probability, retrieval entropy), dust size distribution variables (dust mass-weighted mean diameter MWMD), dust emission temperature, dust composition (quartz, illite, kaolinite, montmorillonite, feldspar and calcite fractions) and the dust columnar mass. The specification of these dust variables follows (roughly) the naming conventions inherited from the dust variables specified in the PSD [AD3]. Geolocation, acquisition time, flags (land, cloud, quality) and global attributes strictly follow the specifications in [AD3].

	aerosol_cci IMARS ATBD	REF : IMARS-ATBD ISSUE : 2.0 DATE : 12.12.2016 PAGE : 40
---	---	---

Table 7.2-1: Dataset names and contained variables of the aerosol_cci IMARS output files.

Format	
	netCDF4
	the products are compliant with CF metadata convention 1.4 http://cfconventions.org/Data/cf-conventions/cf-conventions-1.4/build/cf-conventions.html
Filename	
	<i>Lv2: daily</i> <year><month><day>-ESACCI-L2_AEROSOL-AER_PRODUCTS-IASI_METOPA-DLR-IMARS_<version>-<OrbitalNode>-<StartSensingTime>_<StopSensingTime>-<fv>.nc
	<i>Lv3, daily (total, optional AM/PM):</i> <year><month><day>-ESACCI-L3C_AEROSOL-AER_PRODUCTS-IASI_METOPA-DLR-IMARS_<version>-<OrbitalNode>-<StartSensingTime>_<StopSensingTime>-<fv>.nc
	<i>Lv3, monthly (total, optional AM/PM):</i> <year><month>-ESACCI-L3C_AEROSOL-AER_PRODUCTS-IASI_METOPA-DLR-IMARS_<version>-<OrbitalNode>-<StartSensingTime>_<StopSensingTime>-<fv>.nc
Global attributes	
-2	dateTime = "2009-01-02 11:55:24" (UTC time of first observation)
-1	productID = "Filename"
Auxiliary variables	
1	latitude (at center; for level 3 vector with same value for each line of the data arrays, for level 2 also a complete vector with different values for each pixel)
2	longitude (at center; for level 3 vector with same value for each column of the data arrays, for level 2 also a complete vector with different values for each pixel)
3	time (UTC time of acquisition HHMMSS; one vector for level 2 with pixel acquisition times, two arrays with first and last time of acquisition of any contributing pixel for level 3)
Product variables	
4	D_AOD10000 (dust AOD at 10 μ m)
5	D_AOD10000_uncertainty (dust AOD uncertainty at 10 μ m)
6	D_AOD11000 (dust AOD at 11 μ m)
7	D_AOD550 (dust AOD at 0.55 μ m)
8	D_probability (dust probability)
9	D_REFF (dust effective radius; in μ m)
10	D_MWMD (dust mass-weighted diameter; in μ m)
11	D_mass (dust mass column; in g/m ²)
12	D_temperature (dust layer emission temperature; in K)
13	D_quartz_fraction (quartz abundance in dust; in %)
14	D_illite_fraction (illite abundance in dust; in %)
15	D_kaolinite_fraction (kaolinite abundance in dust; in %)
16	D_montmorillonite_fraction (montmorillonite abundance in dust; in %)
17	D_felspar_fraction (feldspar abundance in dust; in %)
18	D_calcite_fraction (calcite abundance in dust; in %)
Diagnostic variables	
19	satellite_zenith (at center)
20	land_flag (ocean (0) or land (1))
21	cloud_flag (clouds no (0) or yes (1))
22	D_quality_flag (bad (0) through good (1))
23	information_content (retrieval entropy)

	aerosol_cci IMARS ATBD	REF : IMARS-ATBD ISSUE : 2.0 DATE : 12.12.2016 PAGE : 41
---	---	---

8 GENERAL REMARKS AND PRODUCT QUALITY

8.1 Guidelines for product use: confidence levels

Table 8.1-1: Guidelines for application of different levels of quality filtering.

Confidence	Apply filters	Description	Suggested use
Highest quality	$DQF > 3$ and $P_{dust} > 0.5$ and $H < 0.9$ and $\epsilon_{dust} < 40\%$	All quality control filters enabled, yields low number of observations, no interference with cloud contamination	Only if highest reliability level is required, for example: <ul style="list-style-type: none"> • aggregation of mineralogical information • deposition research • analysis of dust radiative effects
High quality	$DQF \geq 3$ and $P_{dust} > 0.5$ and $H < 0.9$	Most quality filters enabled, yields moderately low number of good-quality observations, no interference with cloud contamination	for example: <ul style="list-style-type: none"> • Validation • data assimilation • climatology generation • case studies
Moderate quality	$DQF \geq 3$ and $H < 0.9$	Uses aggregated quality flag and entropy, reasonable number of observations, no interference with cloud contamination	For example: <ul style="list-style-type: none"> • Aerosol-cloud-interaction research • case studies • near-real-time applications
All quality	$AOD > 0$	Passes all dust observations, very high number of observations, potential interference with cloud contamination	for example: <ul style="list-style-type: none"> • manual selection • volcanic ash studies • case studies • retrieval development

The IMARS products are accompanied with a couple of variables for quality control. In general it is possible without any great danger to use the dust AOD wherever retrieved due to the intrinsic quality assurance by the posteriori cloud discrimination scheme (see 5.5). Nevertheless, if one is keen on selecting only high or highest quality observations, it is recommended to use a combination of quality flag, dust probability, dust uncertainty and retrieval entropy for selection. Selecting $DQF \geq 3$ for further use discards those observations with questionable quality. Furthermore if only dust observations with dust probability $P_{dust} \geq 0.5$ and retrieval entropy $H \leq 0.9$ are selected, the reliability of the dust retrieval increases significantly. If furthermore also $\epsilon_{dust} < 40\%$ is selected, only the most

	aerosol_cci IMARS ATBD	REF : IMARS-ATBD ISSUE : 2.0 DATE : 12.12.2016 PAGE : 42
---	---	---

reliable dust observations pass the quality filter. Table 8.1-1 summarizes these guidelines on quality filtering and how the filtering impacts on the selection of observations. All information required for applying tailored quality filtering is directly available from the IMARS files themselves.

8.2 Estimated accuracy from evaluation by the developer

It is not expected that $\varepsilon_{\text{dust}}$ covers the full uncertainty in dust AOD, as especially for dust $\text{AOD}_{0.55\mu\text{m}}$ additional uncertainty is caused by sources not covered by the IMARS retrieval (e.g. absorption at $0.55\mu\text{m}$ by variable iron oxide content, nonspherical effects on $0.55\mu\text{m}$ extinction efficiency which are not covered by AAA, coating or internal mixture with components not accounted for). Nevertheless the accuracy which can be expected from the IMARS scheme based on the selection of optical properties, dust representations etc has been analyzed in some detail in [RD8], (using a previous IMARS version based on principle component decomposition). The analysis showed that the selection of dust optical properties has significant impact on the retrieval accuracy.

Correlation against AERONET coarse mode AOD obtained by the Spectral Deconvolution Algorithm (SDA, [RD43]) was in the order of magnitude of 0.7 while the bias ranged from -0.07 to 0.01. RMSD was 0.17-0.18. about 85% of the 822 coincidences were within 0.2 of AERONET coarse mode AOD from previous versions of IMARS. As the current version of IMARS (v4.2) does no longer exploit principle component decomposition and as optical properties are now determined by AAA instead of determined from Mie theory or measurements, it is not expected that these evaluation results are very representative for the current version.

For IMARS v5.2 the evaluation (by the developer) provides a wide range of accuracy metrics which can be used to assess the quality of the IMARS retrieval. SDA coarse mode AOD observations from 73 stations throughout Asia, Northern Africa, Europe and the Atlantic Ocean have been used for evaluation, covering the full aerosol_cci IASI dust belt region. The developer evaluation has been performed for the year 2009 for the sake of comparability to previously published evaluation results for IMARS. Independent evaluation has to be performed with v5.2 again in order to compare the results to other aerosol_cci retrieval results.

Coincidences are aggregated in a way that for any Metop overpass over a given AERONET station all valid AERONET observations within ± 1 hour of the overpass are averaged and their standard deviation is calculated. Also the coinciding IASI observations are averaged with Gauss-shaped observation weights:

$$\varphi = \exp\left(-\left(\frac{\Delta_{\text{obs}}}{75\text{km}}\right)^2\right) \quad (60)$$

	aerosol_cci IMARS ATBD	REF : IMARS-ATBD ISSUE : 2.0 DATE : 12.12.2016 PAGE : 43
---	---	---

Δobs signifies the distance between the center of the IASI FOV and the station. Consequently the IASI observations closer to the station have higher weight in the averaging than those further away.

Table 8.2-1: Evaluation results for 2009 against AERONET SDA L1.5 observations.

	All	All HQ	All HQ fixed γ	Land	Land HQ	Ocean	Ocean HQ
R_{lin}	0.58	0.70	0.60	0.58	0.69	0.77	0.78
R_{rank}	0.39	0.57	0.53	0.39	0.57	0.61	0.64
R_{like}	0.45	0.53	0.22	0.45	0.53	0.53	0.76
$RMSD$	0.22	0.24	0.43	0.22	0.24	0.16	0.22
$Bias$	-0.02	0.01	-0.28	-0.02	0.01	-0.03	0.00
env_{dyn}	0.13	0.15	0.35	0.13	0.15	0.13	0.17
N	1262	526	526	1256	529	472	95

Table 8.2-2: Evaluation results for 2009 against AERONET SDA L2.0 observations.

	All	All HQ	All HQ fixed γ	Land	Land HQ	Ocean	Ocean HQ
R_{lin}	0.60	0.69	0.58	0.60	0.69	0.75	0.76
R_{rank}	0.40	0.60	0.50	0.40	0.61	0.60	0.59
R_{like}	0.44	0.55	0.22	0.44	0.55	0.53	0.75
$RMSD$	0.23	0.26	0.47	0.23	0.26	0.17	0.22
$Bias$	-0.03	0.00	-0.30	-0.03	0.01	-0.04	0.00
env_{dyn}	0.13	0.15	0.35	0.14	0.15	0.14	0.17
N	1370	537	537	1348	537	451	100

Among the evaluation metrics used here are three correlation estimates: R_{lin} is the classical Pearson correlation, R_{rank} is the Spearman rank correlation and R_{like} is a PDF based likelihood correlation (assuming Gaussian uncertainty distributions) calculated as

$$R_{like} = \frac{\sqrt{e}}{n} \sum_{i=1}^n \left(\exp\left(-0.5 \left(\frac{AOD_i - \tau_i}{\varepsilon_i}\right)^2\right) + \exp\left(-0.5 \left(\frac{AOD_i - \tau_i}{\sigma_i}\right)^2\right) \right) \quad (61)$$

where ε , AOD describe the uncertainty and AOD of the satellite observations and σ , τ the temporal standard deviation and AOD of the ground observations and $i = 1, \dots, n$ enumerates the coincidences. The likelihood correlation is motivated by the standard Pearson correlation, but instead of weighting each observation equally, the observations are weighted by their accompanying uncertainties (averaged from satellite and ground). Consequently higher quality observations (lower uncertainties) are given more weight in the averaging.

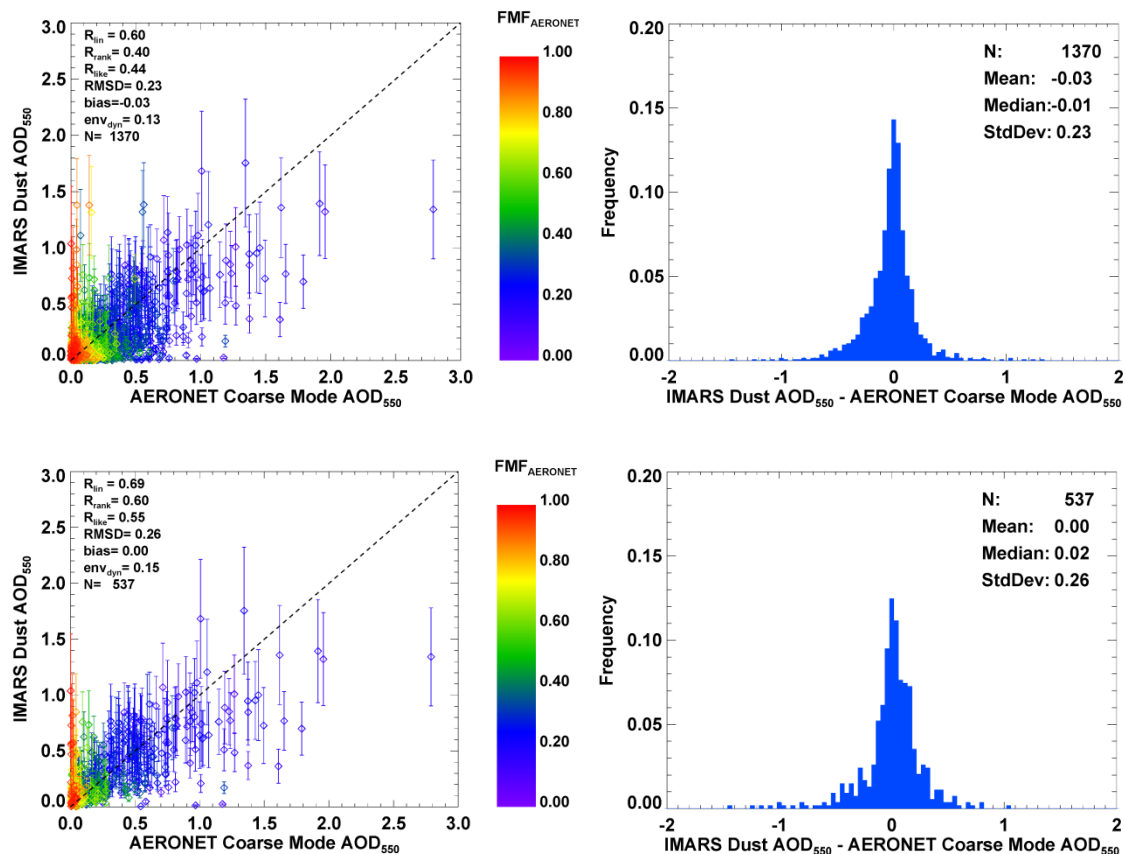


Figure 8.2-1: IMARS dust AOD evaluation results against AERONET SDA L2.0 coarse mode AOD in terms of scatter plots (left) and deviation histograms (right) for all observations (top) and quality-filtered observations (bottom). Observations of 73 AERONET stations for the year 2009 have been used for comparison.

RMSD represents the traditional root-mean-squared difference and the *bias* is the average deviation as usually. env_{dyn} describes the width of the dynamic envelope around the identity, in which $1/e$ of the coincidences are found (as introduced in [RD12]). *N* is the number of coincidences.

Evaluation has been performed for AERONET SDA Level 1.5 (Table 8.2-1) and Level 2.0 (Table 8.2-2) data. The differences between both AERONET levels are marginally in this evaluation. Evaluation metrics have been determined for a range of subsets in order to estimate the impact of quality filtering, size and composition retrieval and surface treatment on the product quality. "All" means all available IMARS observations have been used. "HQ" signifies the quality filtering according to quality level 3 ("high quality", see Table 8.1-1), for "fixed γ " a static VIS-TIR ratio of 1.6 (between $0.55\mu\text{m}$ and $10\mu\text{m}$) has been used independent of retrieved particle size and composition. For "Land" only IASI FOVs over land have been included into the aggregation (eq. (60)), whereas for "Ocean" only FOVs over ocean are included. It is evident that quality

	aerosol_cci IMARS ATBD	REF : IMARS-ATBD ISSUE : 2.0 DATE : 12.12.2016 PAGE : 45
---	---	---

filtering strongly decreases the number of coincidences but increases all evaluation metrics (most significant is the increase in *Rlike*). The retrieval performs a lot better over ocean than over land and the positive impact of the size and composition retrieval is also evident.

Results for all observations and for high quality observations are depicted as scatter plots and deviation histograms exemplarily in Figure 8.2-1. Symbol colour in the scatter plot moreover indicates the fine mode fraction retrieved by the SDA from the AERONET L2.0 observations. The scatterplot RMSD and the histogram standard deviation (StdDev) are mathematically equivalent. In the histograms moreover the median difference between AERONET and IMARS is presented.

Linear regression in the classical definition has not been performed for IMARS and AERONET SDA. It is suggested to use a regression metric similar to the likelihood correlation, which weighs the observations by their uncertainties (as retrieved by satellite and provided by the temporal standard deviation of the ground data). Then the fit

$$\hat{\tau} = a + b \cdot AOD \quad (61)$$

is estimated by

$$b = \frac{\sum_{i=1}^n \exp\left(-0.5\left(\frac{\varepsilon_i}{\langle\varepsilon\rangle}\right)^2\right) \cdot (AOD_i - \langle AOD \rangle) \cdot \exp\left(-0.5\left(\frac{\sigma_i}{\langle\sigma\rangle}\right)^2\right) \cdot (\tau_i - \langle\tau\rangle)}{\sum_{i=1}^n \left(\exp\left(-0.5\left(\frac{\varepsilon_i}{\langle\varepsilon\rangle}\right)^2\right) \cdot (AOD_i - \langle AOD \rangle)\right)^2} \quad (61)$$

$$a = \langle\tau\rangle - b \cdot \langle AOD \rangle \quad (62)$$

where ε , AOD , σ , τ are defined as above.

	aerosol_cci IMARS ATBD	REF : IMARS-ATBD ISSUE : 2.0 DATE : 12.12.2016 PAGE : 46
---	---	---

9 CONCLUDING REMARKS

This Algorithm Theoretical Basis Document describes the physical basis of the Infrared Mineral Aerosol Retrieval Scheme for the IASI instrument on board of the Metop satellites.

The IMARS scheme accounts for surface emissivity and potential cloud contamination. Cloud screening is performed *a posteriori* based on physical reasoning and retrieved cloud and dust probabilities.

The implementation of the retrieval scheme has been described in detail.

The document also describes required input as well as the IMARS output within Aerosol_cci. Auxiliary input data as required by the IMARS algorithm are provided in generic netCDF-4 files. Thus for any experiment it is easy to change for example the optical properties for mineral dust or ice clouds or the set of surface emissivities without the necessity to change the IMARS algorithm or its coded implementation itself. Also the digital elevation model used within IMARS can easily be interchanged.

Initial evaluation results are also presented. These will be updated in consecutive versions of this document by subsequent evaluation within the Aerosol_cci project.

End of the document